Investigation of glass-ceramic composites containing $CeTi_2O_6$ and $CaZrTi_2O_7$ for immobilization of nuclear waste

A Thesis submitted to the

College of Graduate and Postdoctoral Studies

In Partial Fulfillment of the Requirements

For the Degree of Master of Science

In the Department of Chemistry

University of Saskatchewan

Saskatoon

By

Elham Paknahad

Permission to Use

In presenting this thesis in partial fulfillment of the requirements for a degree of Master from the University of Saskatchewan, I agree that the Libraries of this University may make it freely available for inspection. I further agree that permission for copying of this thesis in any manner, in whole or in part, for scholarly purposes may be granted by the professor or professors who supervised my thesis work or, in their absence, by the Head of the Department or the Dean of the College in which my thesis work was done. It is understood that any copying or publication or use of this thesis or parts thereof for financial gain shall not be allowed without my written permission. It is also understood that due recognition shall be given to me and to the University of Saskatchewan in any scholarly use which may be made of any material in my thesis. Requests for permission to copy or to make other uses of materials in this thesis in whole or part should be addressed to:

Head of the Department of Chemistry

University of Saskatchewan

Saskatoon, Saskatchewan S7N 5C9

Canada

Acknowledgements

First of all, I would like to thank my parents who have been the back bone in my personal and academic life for their supports, source of love, strength and encouragement through these years. I am especially thankful to my fiancé who strengthened me in difficult situations. I also thank my sister for being supportive throughout my academic life.

I would like to acknowledge the University of Saskatchewan for supporting me financially. This project was funded by the Natural Sciences and Engineering Research Council (NSERC) of Canada through a Discovery Grant awarded to Dr. Andrew P Grosvenor. I would especially thank to my advisor Dr. Andrew P. Grosvenor for his support, motivation, enthusiasm, guidance and for providing many helpful and beneficial revisions to the written materials throughout my Master study. Besides my advisor, I would like to thank the advisory committee Dr. Thomas Ellis for his insightful comments. I would also thank my past and present group members for giving guidance and especially for sharing the synchrotron beam time. The X-ray absorption spectra in this work were collected with help of Dr. Grosvenor and my group members. I would especially like to thank Dr. Grosvenor and Mohamad Ruwaid Rafiuddin, who helped me collect glancing angle X-ray absorption spectroscopy data presented in Chapter 3.

Mr. Blaine Novakovski and Mr. Tom Bonli (Department of Geology, U of S) are thanked for their help in preparing samples for electron microprobe analysis and performing the measurements. Dr. Zou Finfrock and Dr. Matthew Ward are thanked for their help carrying out XANES and GA-XANES measurements using the 20BM beamline (CLS@APS). Dr. Lucia Zuin is thanked for her support in carrying out XANES experiments using the VLS-PGM (11ID-2)

beamline at the CLS. Dr. Yongfeng Hu and Ms. Aimee Maclennan are thanked for their support in carrying out XANES experiments using the SXRMB (06B1-1) beamline at CLS.

Mr. Jack Hendrix is thanked for carrying out the ion implantation studies using the Tandetron accelerator located at Interface Science Western, University of Western Ontario. I would like to thank all the funding agencies who funded the work in this thesis. The Canadian Foundation for Innovation (CFI) is thanked for providing funds to purchase the PANalytical Empyrean powder X-ray diffractometer that was used in this project. Finally, I owe my gratitude to everyone who have contributed to my thesis production.

Abstract

Glass-ceramic composite materials are being investigated for numerous applications (i.e. textile, energy storage, nuclear waste immobilization applications, etc.) due to the chemical durability and flexibility of these materials. The objective of this thesis was to understand the interaction of brannerite or zirconolite-type crystallites within the glass matrix and to investigate how the local structure of these composite materials changed with changing synthesis conditions as well as to study the structural stability of these materials upon irradiation. Borosilicate and Fe-Al-borosilicate glass-ceramic composites containing brannerite ($CeTi_2O_6$) or zirconolite ($CaZrTi_2O_7$) crystallites were synthesized at different annealing temperatures. Powder X-ray diffraction (XRD) and Backscattered electron (BSE) microprobe images have been used to study how the ceramic crystallites dispersed in the glass matrix. X-ray absorption near edge spectroscopy (XANES) spectra were also collected from all glass-ceramic composite materials. Examination of XANES spectra from the glass-ceramic composites have shown that the annealing temperature, glass composition, and the loading of the ceramic crystallites in the glass matrix can affect the local environment of the glass-ceramic composite materials. Radiation induced structural damage has been simulated by bombarding (implanting) the glass-ceramic materials using 2 MeV Au^- to understand how the structure of a composite wasteform responds to the radioactive decay of incorporated nuclear waste elements. A combination of ion implantation and GA-XANES has been used to investigate the structural stability of glass-ceramic composite materials. Surface sensitive glancing angle XANES (GA-XANES) spectra were collected to selectively probe the damaged surface layer of the ion implanted materials. Examination of Ti K-edge glancing angle XANES (GA-XANES) spectra from ion implanted glass-ceramic composite materials have shown that ion implantation damaged the structure of the ceramics in the composite materials. However, the study

of Si $L_{2,3}$-edge XANES spectra from the ion implanted composite materials showed that ion implantation does not appear to damage the glass structure in these composite materials. A comparison of the glass-ceramic composites containing brannerite or zirconolite crystallites has shown that similar changes in the long-range and local structure of these composite materials occur when the synthesis conditions to form these materials are changed and/or after ion implantation.

Contents

2. Investigation of $CeTi_2O_6$ and $CaZrTi_2O_7$ containing glass-ceramic composite materials

3. Investigation of the stability of glass-ceramic composites containing $CeTi_2O_6$ and $CaZrTi_2O_7$ after ion-implantation

4. Conclusions and directions for future research

List of Tables

List of Figures

List of Figures Appendix A1

List of Abbreviations

APS	Advanced Photon Source
BG	Borosilicate Glass
BSE	Backscattered Electron
CLS	Canadian Light Source
CN	Coordination Number
EDX	Energy Dispersive X-ray spectroscopy
EXAFS	Extended X-ray Absorption Fine Structure
FABG	Fe-Al-borosilicate Glass
GA	Glancing Angle
I_0	Intensity of incident X-ray beam
I_t	Intensity of transmitted X-ray beam
I_f	Intensity of fluorescent photons
ISW	Interface Science Western
PNC/XSD	Pacific Northwest Consortium/X-ray Science Division
SGM	Spherical Grating Monochromator
SRIM	Stopping and Range of Ions in Matter
SXRMB	Soft X-ray Microcharacterization Beamline

SYNROC	Synthetic Rock
t	Sample thickness
TEM	Transmission Electron Microscopy
TEY	Total Electron Yield
VLS-PGM	Variable Line Spacing-Plane Grating Monochromator
XANES	X-ray Absorption Near-Edge Spectroscopy
XAS	X-ray Absorption Spectroscopy
XPS	X-ray Photoelectron Spectroscopy
XRD	X-ray Diffraction
μ	Absorption Coefficient

Chapter 1

1. Introduction

Composite materials can be defined as a combination of two or more materials resulting in better properties than the individual components.[1] Glass-ceramic composite materials (also known as vitroceramics) containing crystalline phases within a glass matrix have received attention for numerous applications in strategic fields such as medicine (bioactive composite as bone replacement and drug delivery systems), photonics, energy storage, aerospace, textiles, and waste management.[2-6] Glass-ceramic materials have the potential to provide significantly higher strength, toughness, low thermal expansion, high chemical durability, isolation capabilities, high resistivity, enhanced thermal stability, and flexibility compared to a glass or cermaic alone.[5-10] These properties can be tailored by controlling the heat treatment of the base-glass composition and/or by controlling crystallization of the base-glass.[11-14]

Glass-ceramics are normally produced in two steps. First, a glass is formed by a glass-manufacturing process. The glass is then cooled and reheated again.[11-14] In the second step, nucleation agents (i.e., ZrO_2, TiO_2, Cr_2O_3 or Fe_2O_3) are added to the base composition of the glass.[11-14] These nucleation agents control the crystallization process. However, only specific glass compositions are appropriate precursors for this method of glass-ceramic preparation; some glasses are too stable and difficult to crystallise and others crystallise too easily resulting in undesirable microstructures.[12-14] The microstructure of a glass-ceramic is typically 50 vol% to 95 vol% crystalline with the remainder being glass.[12-14] Glass-ceramics are attractive as building materials for specialised technical applications requiring a combination of suitable thermo-mechanical properties.[12-14]

1.1. Glass-ceramic composite materials

The first glass-ceramic in the history of materials science without any knowledge of it was discovered by Stookey accidently in 1953.[15] The main crystal phase of this glass–ceramic was lithium disilicate and the base glass was derived from the SiO_2–Li_2O system.[15] The earliest glass-ceramics were produced by a conventional route in which a bulk glass is crystallised by a thermal treatment.[15] A distinct advantage of glass-ceramic composites over other materials is the flexibility in design of a composite to meet specific requirements.[12-14,16]

A powder processing route has recently been developed in which the separately synthesized glass and ceramic materials are mixed and annealed to form glass-ceramic composite materials.[16,17] In this case, highly durable crystalline ceramics are surrounded by the glass matrix.[17] There is a dependency between the viscosity of the glass and nucleation rate (crystallization in the glass matrix) in glass-ceramic composite materials. The viscosity of the glass affects the maximum concentration of the crystalline components and densification of the composite materials.[12-14]

The first commercially viable glass-ceramics were developed by the aerospace industry in the late 1950s.[13] Glass-ceramics were used to protect radar equipment in the noses of aircraft and rockets. Glass-ceramics for the aerospace industry must exhibit a combination of properties from resistance in critical conditions to high mechanical strength.[12-14] Environmental requirements in the aviation and automotive industries have increased the demand for lightweight glass-ceramic composite materials.[12-14]

Glass-ceramics can be pore free compared to sintered ceramics, which make them excellent insulators at high temperatures.[12-14,16] In the development of bioactive glass-ceramics for medical applications, two different types of materials must be addressed that differ in their application environment and preferred properties; glass-ceramic materials for use in implantology (medical

application) and glass-ceramic materials for use in restorative dentistry (dental application).[3,18] Bioactive glass-ceramic composites act as bone replacement and are used in drug delivery systems while glass-ceramics with high mechanical strength are suitable for restorative dental applications.[3,12-14] A low-density and highly bioactive glass-ceramic was developed in 1995.[18] The main crystalline phase of this glass-ceramic material was $Na_2O{\cdot}2CaO{\cdot}3SiO_2$.[18] A wide range of commercially glass-ceramics for consumer applications have been proposed. These materials rely on their relatively high toughness, appealing aesthetics and very low thermal expansion coefficient compared to glass or ceramic alone.[12-14]

1.1.1. Textile application of glass-ceramic composites

Glass companies and the textile industry started to cooperate on the production of fiberglass (a type of fiber-reinforced plastic) in the 1950s. The high strength of certain materials was then discovered by collaboration of glass and ceramic manufacturers.[19-21] Glass-ceramic fibers were subjected to optimized thermal treatments and tested to evaluate their mechanical properties during crystallization.[22] Advanced composites for the textile industry are tailored to perform a specific set of functions in a specific environment. Glass-ceramic composites opened up the area of materials by designing the continuous fibers of high quality which are not randomly oriented like short fibers, but carefully aligned offering high performance for a specific application.[19-23] The textile industry quickly grew and expanded the market of composite materials to a variety of applications.[19-23] The emergence of light-weight glass-ceramic composites from development laboratories offered a variety of uses and increased the mechanical properties of these materials. Glass-ceramic fibers used in high performance composites possess superior mechanical properties compared to normal polymeric fibers. Glass-ceramic composite materials have been considered for textile applications because of the tensile strength, stability, and flexibility of these materials.[19-25]

The overall result is a unique category of glass-ceramic materials with many useful properties and multiple applications ranging from biomedical implants and the textile industry, to hosts for the immobilization of radioactive wastes which will be discussed below.[2-10,12-14,19-21]

1.1.2. The application of glass-ceramic composites for nuclear waste immobilization

The safe and secure immobilisation of nuclear waste is one of the applications that composite materials have received attention for.[4-10] Extensive studies in the field of nuclear waste sequestration have led to the development of wasteforms based on glass–ceramic composite materials.[4-10,26,27] Glass-ceramic composite wasteforms have the potential to provide significantly higher waste loading, enhanced thermal stability, and flexibility compared to glass or ceramic wasteforms alone.[4-10,27,28,29] Glass acts as a secondary barrier for incorporated radioactive actinides in crystalline materials.[4,7,10,17,27,30,31] Investigation of $Gd_2Ti_2O_7$- and $Gd_2Zr_2O_7$-containing glass-ceramic composite materials have shown that the immobilization of nuclear waste vary with changing the glass composition and/or crystalline structure of the composite wasteforms.[4,5,10,17,27,34] Studying the local structure of these materials is a crucial step to the development of these wasteforms for nuclear waste sequestration.[4,7,10,17,30,31]

1.2. Nuclear waste generation and management

Today's technological world is dependent on the availability of energy, including environmentally friendly energy sources. One major source of energy, which has been added to the list of viable energy sources, is nuclear energy.[32] For decades, the nuclear industry has asked the question of what to do with the generated nuclear waste.[33,34]

Large volumes of radioactive waste is generated from spent nuclear fuel, reprocessing of used fuel, and dismantlement of nuclear weapons.[35-38] The main criteria for determining the type of nuclear waste are derived from the radioactive content and half-life of nuclear waste elements

(i.e., the time taken for the elements to lose half of its radioactivity).[35,36,39] Radioactive waste is classified into low level, intermediate and high level wastes. Low-level nuclear waste (LLW) is generated from hospitals, laboratories, industry, and the nuclear fuel cycle. LLW contains 90% of the volume but only 1% of the radioactivity of all nuclear waste.[40] Intermediate-level waste (ILW) contains higher amounts of radioactivity than low level waste. ILW makes up 7% of the volume and only 4% of the radioactivity and is comprised of chemical sludges, nuclear reactor parts, and contaminated materials from reactor.[40,41] High level radioactive waste (HLW) produced either by the reprocessing of nuclear spent fuel or by nuclear weapons programs must be efficiently isolated from the biosphere.[41] High level nuclear waste accounts for 95% of the total radioactivity generated in a nuclear reactor. This type of nuclear waste is dangerous, so it is important to find safe and secure ways to dispose of HLW.[41]

Canada has produced nuclear waste since the early 1930's.[42,43] With increasing demand for nuclear energy, a significant amount of nuclear waste has been produced over the years. The generated nuclear wastes can then be managed and stored at reactor sites.[42-45] There are several storage methods to immobilize hazardous nuclear waste from the environment safely and securely. A spent fuel storage pool is one option that can be used to store spent nuclear fuel rods discharged from nuclear reactors. The spent fuel rods are placed under water (~20 feet of water) with continual monitoring for ~5-10 years to reduce the heat generated from the radioactive waste elements.[42-45] The spent fuel rods are then sent to dry cask storage sites that are surrounded by inert gas (typically He). These casks are cylinders made of steel/copper and covered by concrete layers to protect radioactive waste from the environment.[42-45] In Canada, nuclear waste is stored in either storage pools or dry casks. However, these sites are considered short term storage methods to immobilize nuclear waste.[42-45]

Finding permanent ways to dispose of radioactive waste with longer half-lives has become a crucial issue in our industrialized society.[46-48] It has been proposed to dispose nuclear waste deep under ground (i.e., below sea level) for long term storage, which is called geological sequestration.[46-48] Geological sequestration is still under consideration because of the role of public policy and political issues.[47,49,50] Considering highly durable materials as wasteforms for isolation of radioactive waste elements can be another option for long-term storage.[4-10] The choice of immobilization technology depends on the physical and chemical nature of the waste and wasteform as well as the criteria for long-term storage and disposal facilities.[42-45]

1.3. Nuclear wasteforms

Nuclear wasteforms are materials that can safely and securely incorporate various radioactive waste elements.[26] Extensive studies in the field of nuclear waste sequestration have lead to the development of wasteforms based on crystalline ceramics,[51-53] amorphous glasses,[54,55] or glass–ceramic composite materials.[4-10,17,27,34] There are general requirements for wasteforms which incorporate nuclear waste elements including high waste loading, easy processing, high radiation stability, and chemical durability over thousands of years.[4-10,17,26,27,34]

1.3.1. Radiation effects on nuclear wasteforms

The long-term stability and durability of nuclear wasteforms can be affected by radioactive decay of incorporated nuclear waste elements.[34,56-59] The incorporated radioactive waste elements can release α-particles (β-particles or γ-rays can also be released) depending on the decay mechanism over a period of time and transform to daughter products. The α-particles have a significant ionising effect and the daughter products have a sufficient recoil energy which cause large displacement in the structure of a material through both elastic and inelastic collisions of atoms.[34,56-59] Radioactive decay events can result in the development of defects, swelling, and

cracking of the wasteform and can lead the structure to become metamict (i.e., the structure becomes amorphous).[34,56-59] Therefore, it is important to understand how the structure of a wasteform responds to the radioactive decay of incorporated nuclear waste elements.[34,56,59-61] Investigating the long-term radiation damage (i.e., metamiction) of a wasteform is not possible on a real time scale (i.e., 10^3-10^6 years).[34,56-59] However, radiation induced structural damage can be simulated by bombarding (implantation) materials with high-energy ion beams (e.g., Au^-, Kr^+, and Xe^+).[34,56,60,61] A number of stable and durable materials have been proposed as wasteforms such as glass, ceramic, multiphase systems, and glass-ceramic wasteforms, which will be discussed below.[6-10,26,27,34,60-63]

1.3.2. Glass wasteforms

Silica glass was proposed and developed as the first host material for nuclear waste sequestration.[54,55,64,65] Vitrification is achieved by embedding or loading of nuclear waste elements within the glass matrix at low melting temperatures.[54,55] The ability of a glass to incorporate a wide range of nuclear waste elements (both minor actinides and fission products), the stability of glass against chemical perturbations, and the ease of industrial scale processing have validated the choice of glass as a suitable wasteform.[54,55] One of the most positive features of the vitrification method is that glasses are immune to amorphization by radiation induced structural damage as these materials are, by nature, amorphous.[64] However, ceramic wasteforms can exhibit higher thermal stability and enhanced waste loading than vitrified wasteforms.[27,34,51-53] It was reported that most actinide elements (e.g., Pu) can only dissolve in a glass network at very low loadings (3-10 wt %).[65]

There are three categories of oxides in glass that depend on their role in the glass network: network formers which form the interconnected backbone glass networks (e.g., B, Fe, P, etc),

network modifiers which can break up the glass network and form ionic bonds with nonbridging oxygens (e.g., Na, K, Ca, etc.), and intermediates which can behave as a network former or a network modifier (e.g., Ti, Zr, Al, etc).[8,62,66,67] Radioactive nuclear waste elements can bind to glass former elements (e.g., Si) via bridging O bonds in a glass matrix.[34] Glass wasteforms can have a wide variety of compositions including silicate glasses, borosilicate glasses, and phosphate glasses.[5,54,55,66,67]

1.3.2.1. Borosilicate glasses

Borosilicate glass, known under trade names such as Pyrex and Duran, is widely used in industry because of the high chemical resistance and the low thermal expansion coefficient of this glass. [54,55,64,65,68] Borosilicate glass is produced by adding boric oxide to the traditional glass formers of silica, soda, and ground lime and was proposed as a first generation wasteform for the immobilisation of high level nuclear waste (HLW) due to the stability and flexibility of the silicate network.[5,54,55,66-68] Previous investigations of borosilicate glasses have shown that the nuclear waste loading and the resistance to radiation induced structural damage can depend on the glass composition.[5,54,55,68] Although borosilicate glasses as nuclear wasteforms can accommodate a wide range of waste elements, these materials have some disadvantages including loading limit of actinide elements and the volatility of some fission products during vitrification.[34,64-68]

1.3.2.2. Fe-Al borosilicate glasses

Aluminosilicate is one important type of glass and contains 20 wt% aluminium oxide (alumina-Al_2O_3).[17,27,34] It has been suggested that the presence of transition metals (e.g., Fe) in borosilicate glass can increase the structural stability of these wasteforms.[69-71] The release of β-particles and γ-rays from radioactive elements can lead to the formation of electron-hole pairs in the glass wasteforms and the presence of Fe in the glass has been suggested to be able to trap these

electron-hole pairs.[69,71] This can lead to the materials having an increased resistance to radiation induced structural damage.[17,69,71]

1.3.3. Ceramic wasteforms

Ceramic wasteforms are promising hosts for nuclear waste immobilization because of increased waste loading and chemical durability compared to conventional glass wasteforms.[51-53,72-77] Many types of ceramics have been proposed as candidates for immobilisation of nuclear waste such as brannerite ($CeTi_2O_6$), zirconolite ($CaZrTi_2O_7$), hollandite ($BaAl_2Ti_6O_{16}$) and pyrochlore ($A_2B_2O_7$).[29,34,57,72,77] These ceramics are considered to be attractive options for the long-term storage of actinides in geological repositories.[72,77,78] Investigations of ceramic wasteforms have shown how a variation in the long-range order of ceramics can affect the chemical durability and structural stability of these materials.[29,34,57,72,78] The main drawback of using ceramic materials as nuclear wasteforms is that ceramics can only incorporate a limited number of radioactive waste elements in specific atomic positions of the crystal structure compared to glass wasteforms.[29,34]

1.3.3.1. Brannerite ($CeTi_2O_6$)

Titanate ceramics are one option for HLW sequestration applications.[29,34,57,79] Brannerite, having the composition MTi_2O_6 (M = U, Th, Ce), is one possible host matrix for the immobilization of actinide-bearing radioactive waste.[80-83] The brannerite crystal structure belongs to the monoclinic system, with space group C2/m. The structure consists of alternating columns of edge-sharing MO_6 octahedra with regular shapes and distorted layers of edge-sharing TiO_6 octahedra that are corner sharing with the MO_6 octahedra (Figure 1.1a).[80,81] Cerium acts as an actinide simulator element in MTi_2O_6 because Ce has a similar ionic radius, coordination environment, and electronic structure to some actinide elements.[81-83] Cerium is not a good simulator element for U because Ce can be easily reduced to Ce^{3+} while U^{3+} is rare; however, Ce

is a good simulator element for Pu.[81-83] Moreover, the crystalline structure of brannerite (MTi_2O_6) is a good example for immobilizing uranium-bearing radioactive waste because UTi_2O_6 can hold a significant concentration of uranium (~55 wt% per formula unit).[82,83]

1.3.3.2. Zirconolite ($CaZrTi_2O_7$)

Zirconolite-based ceramics are considered as one of the most promising wasteforms for HLW sequestration applications.[85,86] Previous studies have demonstrated that zirconolite can immobilise both actinides and fission products in the crystal lattice for the long term.[87,88] Zirconolite refers specifically to $CaZrTi_2O_7$, which has a monoclinic structure (space group C2/c). The zirconolite crystal structure is made up of layers of TiO_6 and TiO_5 polyhedra linked to form a monoclinic system with Ca^{2+} (8 coordinate) and Zr^{4+} (7 coordinate) ions being found in the large interstitial sites between these layers (Figure 1.1b).[89,90]

1.3.4. Multi-phase ceramic wasteforms

The SYNROC strategy aims to immobilise radioactive wastes in durable multiphase ceramics based on the stable natural titanate minerals that have immobilized uranium and thorium for millions of years.[34,72,79,91,92] SYNROC is a particular kind of "Synthetic Rock" invented in 1978.[34,72,79,91,92] The main minerals in SYNROC are hollandite ($BaAl_2Ti_6O_{16}$), zirconolite ($CaZrTi_2O_7$), and perovskite ($CaTiO_3$). Zirconolite and perovskite can incorporate long lived actinides such as plutonium (Pu), while hollandite principally immobilises cesium (Cs), along with potassium (K), rubidium (Rb) and barium (Ba).[72,79,91,92] Different forms of SYNROC have been developed to deal with radioactive waste particularly military radioactive waste, including a substantial amount of plutonium (Pu).[72,79, 92]

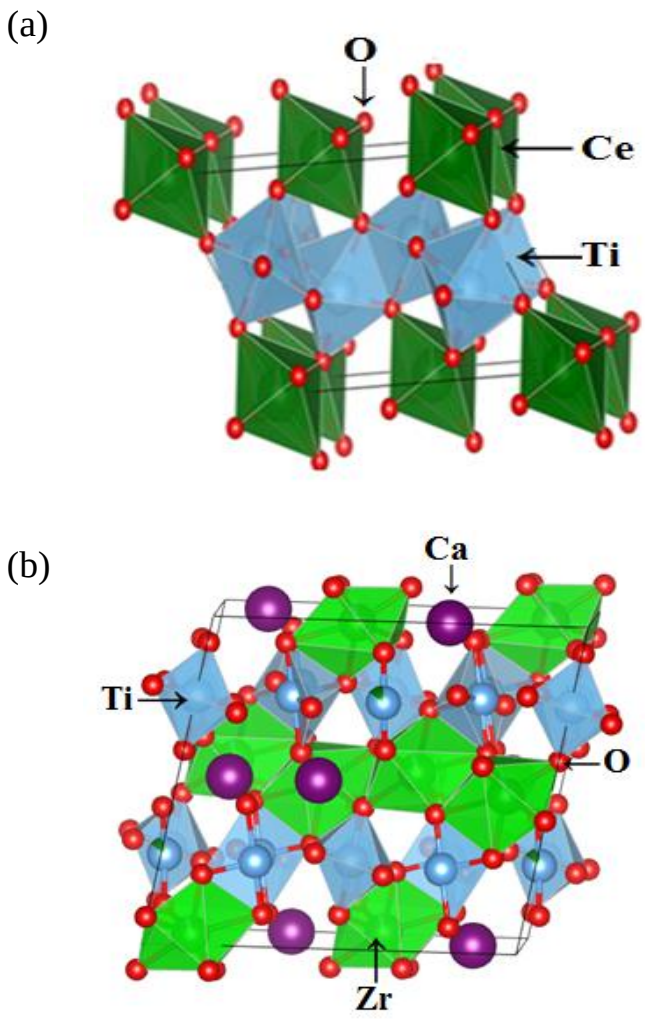

Figure 1.1. The monoclinic crystal structures of (a) $CeTi_2O_6$ and (b) $CaZrTi_2O_7$ are shown. The structures were generated using the VESTA program.[84]

Although glass (i.e., silicate glass or borosilicate glass) is an appropriate host for a large fraction of HLW, considerable quantities of waste still exist that are very difficult to incorporate in glasses so multiphase ceramic materials have been proposed and designed to incorporate a wide range of complex nuclear waste elements. Waste loadings of 50-70 wt% have been incorporated into highly durable SYNROC materials.[72,92] To achieve maximum cost saving and optimum performance, SYNROC waste forms are tailored to suit the particular characteristics of the nuclear

waste to be stored.[72,79,91,92] Pyrochlore-rich SYNROC can be used to immobilize nuclear waste with a loading of 50 wt % U/PuO_2.[93,94] Zirconolite is similar to pyrochlore and can incorporate up to 50% by mass of PuO_2 and/or UO_2.[93,94]

1.3.5. Glass-ceramic wasteforms

Glass-ceramic materials are considered as wasteforms with a variety of appropriate properties for specific applications at low cost.[2-10,27-29,34] These materials are of interest because of the possibility of enhancing the incorporation of nuclear waste elements based on the combination of glass and ceramic materials.[4,10,17,27,29,34] SYNROC-glass combinations can be tailored for a wide range of radioactive waste, where the actinide elements are typically incorporated into extremely durable crystalline titanate phases such as zirconolite or pyrochlore within a glass matrix.[4,5,10,17,27,29,34] Glass-ceramic composite materials have the ability to incorporate actinides and various fission products in either the crystalline structure or the glass matrix.[4,5,10,17,27,29,34] Studies of glass-ceramic composite materials containing $Gd_2Zr_2O_7$ and $Gd_2Ti_2O_7$ have shown how the ceramic crystallites interact within the glass matrix and how the long-term structural stability of these materials can be affected upon radioactive decay of incorporated nuclear waste.[4,5,10,17,27,29,34] Investigating the compositional and structural stability of glass-ceramic composite materials has led to the development of these materials for nuclear waste sequestration.[4,5,10,17,29,34,57,59] It is important to investigate how the local structure of these materials changes depending upon glass/ceramic composition or as a result of radiation induced structural damage, which can be simulated by ion implantation.

1.4. Ion beam implantation studies

Investigating the long-term radiation damage (i.e., metamiction) of a wasteform is not possible on a real time scale (i.e., 10^3-10^6 years). However, radiation induced structural damage

can be simulated by bombarding materials with high energy ion beams.[34,56-61] Different ions (e.g., Au^-, Kr^+, Xe^+ and etc.) at various doses have been implanted to mimic radioactive decay of incorporated radioactive waste elements in nuclear wasteforms.[56-61,95-97]

A typical ion beam implantation chamber consists of a sputter ion source, accelerator, and a target chamber. An ion beam implantation chamber from a Tandetron accelerator (located at Interface Science Western (ISW), University of Western Ontario, London) is shown in Figure 1.2.[98] The sputter ion source is a ion source that generates high intensity ion beams from elements. The ion beams are accelerated to high energies (MeV) using accelerator tubes.[98] A uniform amount of ions with a specific velocity and charge are transferred to the target chamber (where the sample is placed) using high-energy magnets and slits. During implantation, the ion beam is aligned approximately normal to the surface of a sample (i.e., pellet).[98] Finally, the ions are implanted on a target sample and measured in terms of dose or flux (ions/cm^2). The high-energy ion beam can penetrate to a maximum depth of 450-1000 nm. The penetration depth depends on composition, ion beam energy, and the ion species.[98]

1.5. Characterization techniques

In order to successfully probe the long-range and local structure of glass-ceramic materials, a variety of characterization techniques (i.e., powder X-ray diffraction, electron microscopy and X-ray absorption near-edge spectroscopy) were utilized in this thesis. It should be mentioned that this study mainly focused on examination of the bulk region of the glass-ceramic composite materials. This section discusses the synchrotron radiation techniques that were used to investigate the glass-ceramic composite materials.

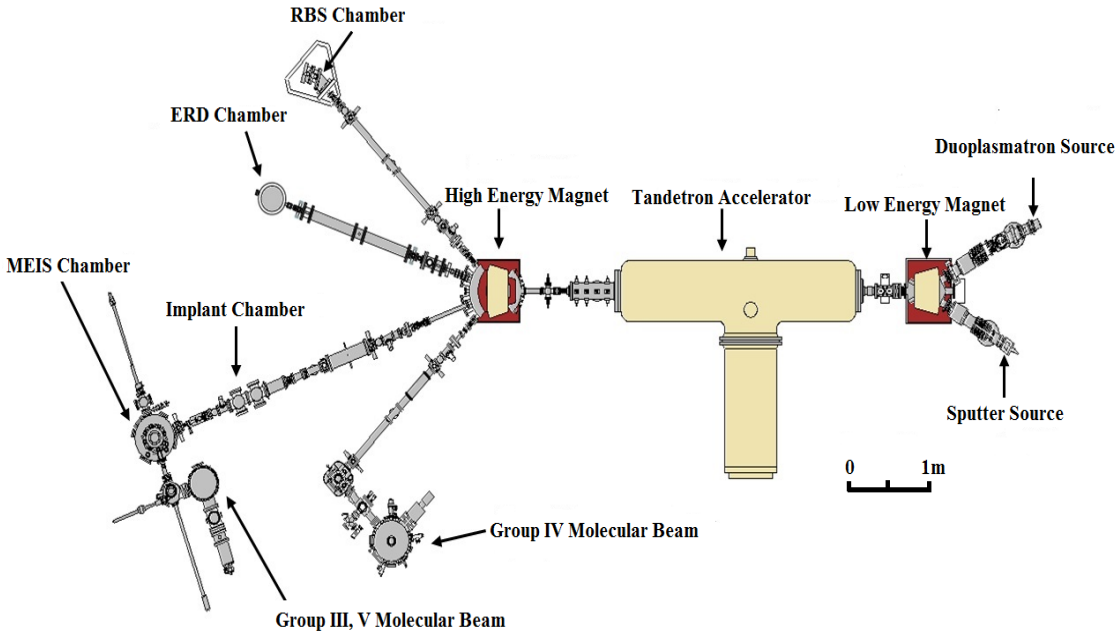

Figure 1.2. Schematic diagram of the Tandetron accelerator along with the ion implantation chamber located at Interface Science Western (ISW), University of Western Ontario is shown.[98] The diagram was adapted from the ISW website.[98] High energy (MeV) ions are generated from a sputter source, accelerated through an accelerator, and transferred to an implantation chamber.

1.5.1. Synchrotron radiation techniques

In this thesis, X-ray absorption spectroscopy (XAS) experiments have been used to probe the local structure of the materials. XAS requires the use of a synchrotron facility (i.e., Canadian Light Source in Saskatoon, SK). Synchrotron facilities provide a broad energy band and allow access to an extensive range of spectroscopic techniques from far-infrared light ($\lambda < 15$ μm; $E <$ 80 meV) to hard X-rays ($\lambda < 30$ pm; $E > 40$ keV).[99-101]

A schematic diagram of a modern synchrotron radiation source is shown in Figure 1.3.[101] Synchrotron radiation is a highly polarized, narrow monochromatic beam with a high intensity.[99-102] Synchrotron facilities create light using electrons. These electrons are generated in multiple steps. First, an electron gun attached to a linear particle accelerator is used to generate and

accelerate electrons to a high velocity and high energy (MeV).[99] Following this, the electrons are injected in bunches and accelerated to a relativistic speed and high-energy (GeV) in an evacuated booster ring. The accelerated electrons in the booster ring are then injected into the polygon shaped closed loop called the storage ring.[99] The storage ring consists of bending magnets and insertion devices, which are responsible for the generation of the most intense synchrotron radiation. Circulating electrons in the storage ring will generate very intense electromagnetic radiation. The generated synchrotron radiation in the storage ring is then delivered to the end station through beamline sections.[99]

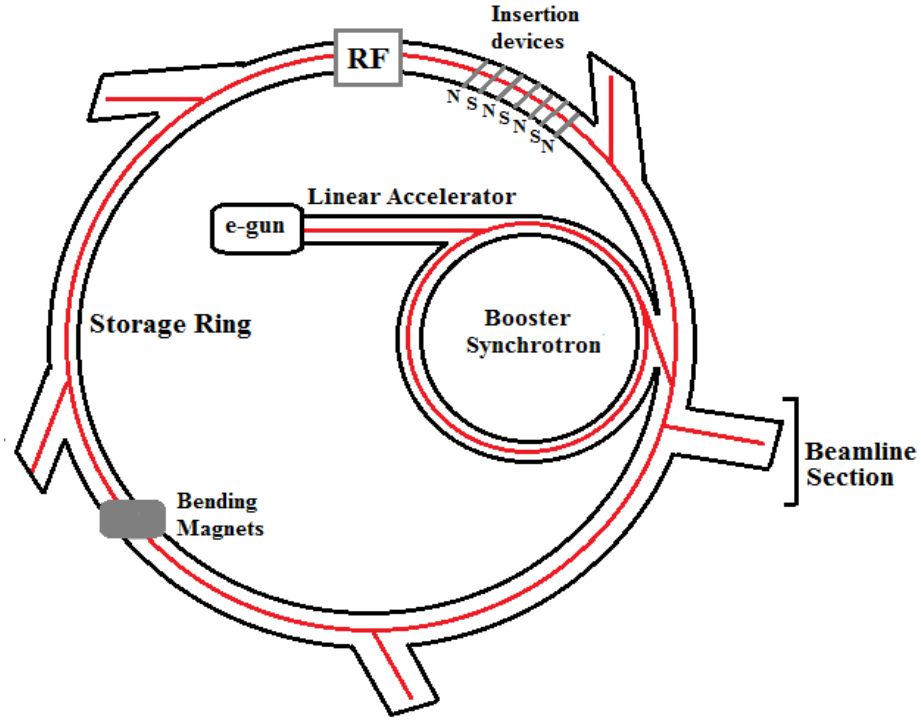

Figure 1.3. Schematic diagram of a modern synchrotron source is shown.[99-101] The electrons are accelerated with a relativistic speed using a series of accelerators: Linear accelerator, booster ring, and storage ring, respectively. The beamlines bring the synchrotron radiation to the experimental chamber using various optical devices.

1.5.2 Beamline set-up

A beamline consists of various optical instruments to produce collimated and monochromated beams depending on the X-ray energy range and the measurement method (i.e., spectroscopic methods).[99] A front end aperture is the fisrt part of a beamline that brings the beam from the storage ring to the beamline. Optics are then used to select the wavelength of a beam, and finally the beam goes to an experimental chamber.[99] The end stations for a beamline vary with the measurement method (i.e., spectroscopy, scattering, and imaging).[99]

The monochromated beams are focused on the sample with optimized photon flux and good energy resolution in order to perform X-ray absorption spectroscopy experiments.[99,100,103-107] Double crystal monochromators and mirrors are used for hard X-rays (i.e., E > 2 keV) to select the energy and to collimate the X-ray beam onto the sample, respectively.[100,108] Double crystal monochromators have two single crystals mounted parallel to each other with one used to select the energy and the other to track the position of the beam spot on the sample.[103-106] In soft X-ray measurements, diffraction gratings can cause separation of light with different wavelengths (dispersion) and high energy resolution of the soft X-rays can be achieved by large dispersion and small focus.

1.5.3. XAS experimental set-up

In a XAS experiment, the absorption coefficient (μ) from a sample is measured as a function of the incident photon energy. The absorption coefficient can be determined either by measuring the intensities of incoming and transmitted beam or by measuring the intensities of the incoming beam and emitted photons/electrons.[103-106] XAS in transmission measurements follows the well known Beer-Lambert law.

$$\ln\left(\frac{It}{I_0}\right) = -\mu t \tag{1.1}$$

'I_0' is the incident X-ray beam intensity, 'I_t' is the transmitted intensity through the sample, 't' is the sample thickness and 'μ' is the sum of the absorption coefficients of all components in a sample.[103-106] In transmission mode, the incident X-ray beam (I_0) passes through a sample of thickness t, and the transmitted beam (I_t) is measured (see Figure 1.4 a).[104,106,107]

Different detection methods can be used to collect a XAS spectrum. The preferred detection methods rely on the absorption-edge energy and sample environment.[108-111] A schematic diagram of different detection methods for X-ray absorption spectroscopy is shown in Figure 1.4. For hard X-ray XAS measurements, transmission and fluorescence yield (FY) are the most common detection methods, while in soft X-ray XAS measurements, total electron yield (TEY) and fluorescence yield (FY) are generally used.[109-111] Transmission mode is not typically used in soft X-ray measurements because soft X-rays cannot fully penetrate and transmit through the thick samples.[109-111] Fluorescence yield spectra are typically measured either as the total fluorescence yield (TFY; sums over the whole energy range) or as the partial fluorescence yield (PFY; selectively detects the fluorescence from a narrower energy range). Transmission, florescence, and electron yield measurements have different sampling depths.[103-106,108,109] Transmission and fluorescence measurements are inherently bulk sensitive whereas total electron yield measurements are surface sensitive because of the shorter mean free path of electrons versus photons.[104,108,110,113]

The total electron yield measurements are sensitive to charging effects.[110] Charging effects obstruct the transfer of electrons from grounded sample holder to the surface area of thick insulating samples. The fluorescent measurements can be strongly affected by absorption or

saturation effects in thick or concentrated samples.[112,113] Applying effective methods in sample preparation and/or mounting procedure can reduce these problems significantly.[108-111]

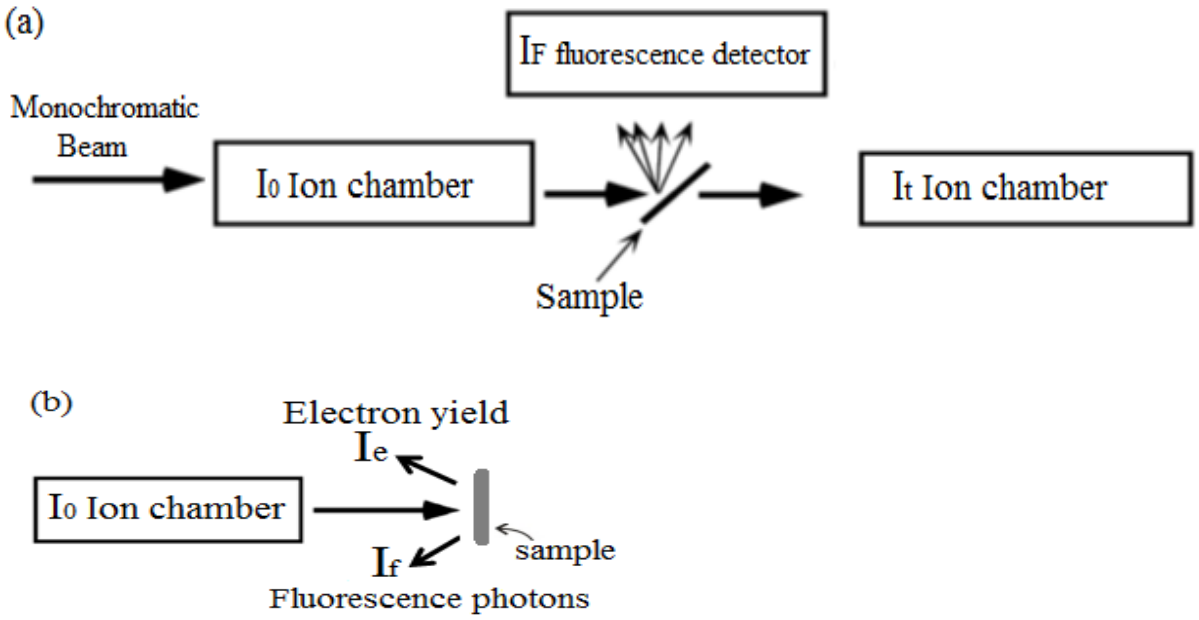

Figure 1.4. A schematic diagram of different detection methods of X-ray absorption spectroscopy. (a) Hard X-ray transmission and fluorescence set-up. The transmitted beam is measured using an ionization chamber (I_t) and the released fluorescence photons (I_f) are collected using fluorescence detector. (b) Soft X-ray total electron yield (TEY) experiments are performed in vacuum. A total electron yield spectrum along with the fluorescence spectrum can be collected simultaneously to get accurate XANES spectra.

1.6. An overview of XANES

X-ray absorption spectroscopy (XAS) is a powerful technique that can be used to investigate changes in the local structure of materials and can be applied not only to crystalline but also amorphous systems like glasses.[103-106,111,114] XAS is element specific and sensitive to the oxidation state, bonding environment, and local geometry around the absorbing atom.[103,104,111,114] In XAS, a core electron from occupied atomic/molecular orbitals is excited into unoccupied orbitals above the Fermi level (conduction and/or continuum states) by the absorption of an

incident (X-ray) photon (see Figure 1.5 a).[103-106,114-116] A typical XAS spectrum can be divided into two main regions: the XANES (X-ray absorption near edge spectroscopy) region, which extends from ~5 eV below the absorption edge (pre-edge) to ~50 eV above the edge, and the EXAFS (extended X-ray absorption fine structure) region which extends beyond ~50 eV above the absorption edge (see Figure 1.5 b).[103-106,114-116] The XANES region, which is the main focus in this thesis, can provide detailed information about the coordination environment and oxidation state of the absorbing atom. The EXAFS region, however, provides information on single and multiple scattering events of an excited core-electron with neighbouring atoms and, through analysis of the fourier transform of the spectrum, can provide information on the local structure around the absorbing atom.[103-106]

The notation used to label X-ray absorption edges depends on the shell that the electron is excited from. For example, the excitation of an electron from a 1s orbital is labeled as the K-edge (see Figure 1.5 a).[103-106,110,111,114-116] The electronic transitions in XANES spectra directly probe the angular momentum of the unoccupied electronic states and, therefore, should follow the conservation of angular momentum (i.e., $\Delta l = \pm 1$). The prominent transitions in the K-edge are from dipolar transitions (1s→np); however, quadrupolar transitions (i.e., $\Delta l = \pm 2$, 1s→(n-1)d), which are not allowed by the conservation of angular momentum, may be observed in K-edge XANES spectra.[103-106, 114-116]

In this work, materials were investigated by collecting K-edge XANES spectra (excitation of 1s electrons) and L-edge XANES spectra (excitation of 2p electrons). The L_1-edge XANES spectra consists of 2s→np transitions whereas $L_{2,3}$-edge XANES spectra contains 2p→(n-1)d transitions (see figure 1.5 a).[103-106,114-116] A transition metal (i.e., Ti) K-edge XANES spectrum is shown in Figure 1.6, which consists of a low intensity pre-edge (A) feature (1s→3d; electric

quadrupolar transitions) and very high intensity main edge (B,C) feature (1s→4p; electric dipolar transitions).[17,117-120]

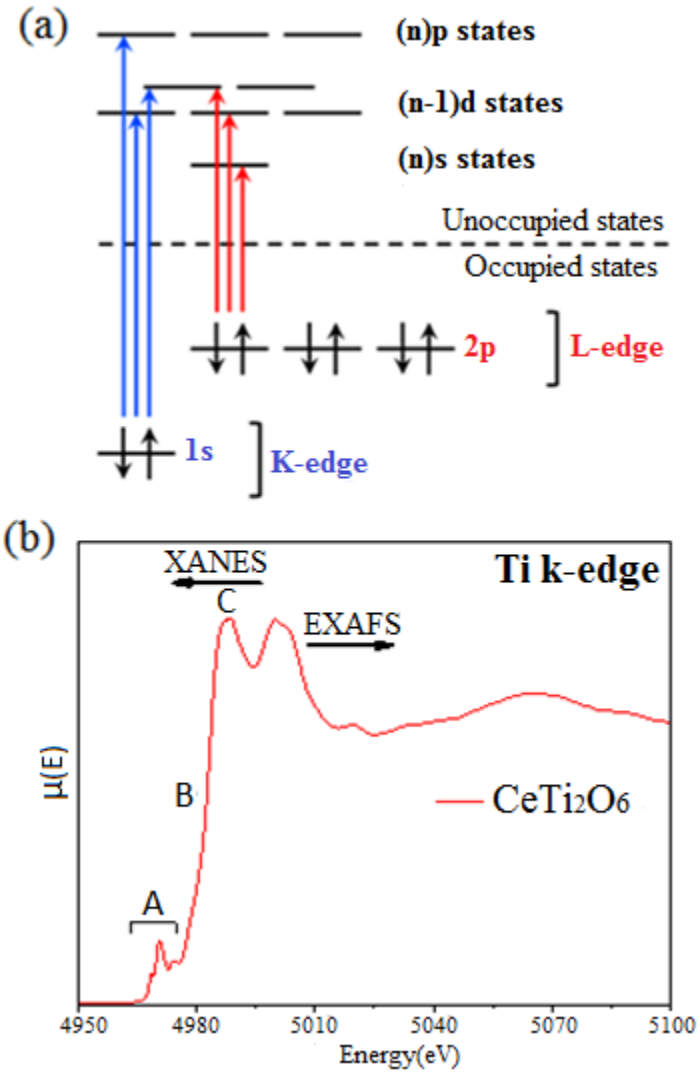

Figure 1.5. (a) A representative energy diagram for electron transitions in the XAS process. Metal K-edge transitions include electric dipole allowed transitions (1s→np) and quadrupole transitions (1s→(n-1)d). In the L-edge, the dipole allowed electronic transitions are 2s→np (L_1-edge) and 2p→(n-1)d ($L_{2,3}$-edge). (b) Transition metal (Ti) K-edge XANES spectrum along with EXAFS from $CeTi_2O_6$ is shown. The XANES spectrum is divided into pre-edge (A:1s→3d) and main-edge (B,C:1s→np) regions.

The electric quadrupolar transition (pre-edge (A)) is normally forbidden by selection rules (conservation of angular momentum) but it becomes allowed with mixing of d and p orbitals.[117-120] An increase in the intensity of the pre-edge peak is observed for a site without a center of symmetry (i.e., TiO_4 tetrahedran or a TiO_5 square pyramid) because of the mixing of 3d and 4p orbitals, which provides some dipole allowed character to the quadrupolar transition. As shown in Figure 1.6, decreasing the coordination number ($Ti^{[6]} \rightarrow Ti^{[5]} \rightarrow Ti^{[4]}$) can increase the intensity of the pre-edge feature (A). The low energy pre-edge feature (A) and the high energy main-edge features (B,C) are sensitive to the coordination number, bonding environment, and the oxidation state of the metal atom.[17,117-120]

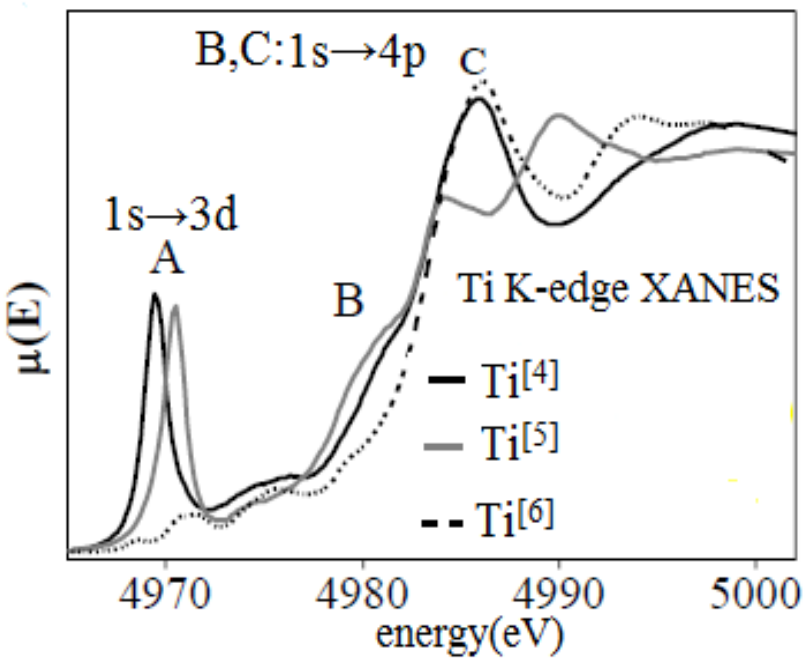

Figure 1.6. Ti K-edge XANES spectra of materials having 4-, 5-, and 6-coordinate Ti atoms. The figure was retrieved from reference 118. The intensity and energy of pre-edge peak (A) are observed to change significantly with varying CN. These changes are also accompanied by changes in the main-edge features (B,C).

1.6.1 Glancing angle XANES

A special XANES technique that can be used to investigate the resistance of nuclear wasteforms to radiation induced structural damage is glancing angle XANES (GA-XANES).[89,95-97] Glancing angle XANES is a surface sensitive technique that can be used used to probe only the damaged surface layer of a material (typically only a few hundred nm thick).[89,121-123] In a glancing angle experiment, the incident X-ray beam angle (generally called the glancing angle) is set to be just above the critical angle of total external reflection to selectively probe the surface layer of materials.[89,121-123] If the incident X-ray angle is set to be less than the critical angle, total external reflection occurs and X-rays propagate parallel to the surface of the material. GA-XANES spectra become more surface sensitive when the X-ray beam angle of incidence on the surface of a material decreases.[89,121-123] The X-ray attenuation depths depend on the density of a material and the excitation energy (i.e., absorption-edge energy).[122]

1.7. Thesis objectives

The objectives of this thesis were to investigate how the local structure of glass-ceramic composite materials change as a result of synthesis conditions and to study the structural stability of these glass-ceramic materials upon irradiation. Borosilicate and Fe-Al-borosilicate glass-ceramic composites containing brannerite ($CeTi_2O_6$) or zirconolite ($CaZrTi_2O_7$) crystallites were synthesized at different annealing temperatures. Electron microscopy and powder X-ray diffraction (XRD) have been used to study the dispersion of ceramic crystallites in the glass matrix. X-ray absorption near-edge spectroscopy (XANES) was used to investigate changes in the local structure of these materials by collecting Ti K-, Ce L_3-, Zr K-, Si $L_{2,3}$-, Fe K-, and Al $L_{2,3}$- edge XANES spectra. Radiation induced structural damage has been simulated by bombarding (implanting) the glass-ceramic materials using 2 MeV Au^- ions to understand the effect of

radioactive decay of incorporated actinide elements on the wasteforms. This thesis has also demonstrated the ability of GA-XANES to probe the damaged surface layer of ion implanted composite materials. This work will contribute to a better understanding of the long-range and local structure of these composite materials when the synthesis conditions to form these materials are changed and/or after ion implantation.

Chapter 2

Investigation of $CeTi_2O_6$ and $CaZrTi_2O_7$ containing glass-ceramic composite materials*

2.1. Introduction

Glass-ceramic composite materials containing crystalline phases within a glass matrix are being investigated for nuclear waste immobilization applications due to the chemical durability and flexibility of these materials.[4-10] Glass-ceramic composite wasteforms have the potential to provide significantly higher waste loading, enhanced thermal stability, and flexibility compared to glass or ceramic wasteforms alone.[4-10,17,27,29,34] Glass-ceramic composite materials have the ability to incorporate actinides and various fission products in either the crystalline structure or the glass matrix. For example, radioactive waste elements incorporated in the highly durable crystalline phase within the glass matrix would benefit from a double barrier (ceramic + glass).[4,7,10,17,27,29,34] Investigations of the compositional and structural stability of the glass-ceramic composite materials have led to the development of these materials for immobilization of nuclear waste.[4–10,17,27,29,30,31,34]

The objective of this study was to understand how ceramic crystallites interact within a glass matrix, and to investigate how the local structure of these composite materials change as a result of synthesis conditions. Borosilicate and Fe-Al-borosilicate glass-ceramic composites containing brannerite ($CeTi_2O_6$) or zirconolite ($CaZrTi_2O_7$) crystallites were synthesized at different annealing temperatures to study the effect of composition and annealing temperature on

* A version of this Chapter has been published. Reprinted with permission from Paknahad, E.; Grosvenor, A. P. *Can. J. Chem*. **2017**, In Press © dx.doi.org/10.1139/cjc-2016-0633

the local and long-range structure of these materials. Electron microscopy and powder X-ray diffraction (XRD) have been used to study the dispersion of ceramic crystallites in the glass matrix. X-ray absorption near-edge spectroscopy (XANES) was used to investigate changes in the local structure of these materials by collecting Ti K-, Ce L_3-, Zr K-, Si $L_{2,3}$-, Fe K-, and Al $L_{2,3}$- edge XANES spectra.

2.2. Experimental

2.2.1. Synthesis

Brannerite was synthesized using the ceramic method. CeO_2 (Alfa Aesar, 99.9%) and TiO_2 (anatase, Alfa Aesar, 99.6%) powders were mixed in stoichiometric amounts, pelleted at 6 MPa and heated in air for six days at 1325 °C with intermediate mixing and pelleting. Zirconolite, nominally $CaZrTi_2O_7$, was also synthesized by the ceramic method using a stoichiometric mixture of CaO, ZrO_2 (Alfa Aesar, 99.7%), and TiO_2 (rutile, Alfa Aesar, 99.9%) powders. Calcium carbonate ($CaCO_3$, ACS, >99%) was heated in air first at 900 °C for one day to decompose to CaO. $CaZrTi_2O_7$ was synthesized by mixing the binary oxides using an agate mortar followed by pressing the mixture into a pellet using a pressure of 6 MPa, and then heating the pellet in air for two days at 1400 ^oC. The sample was then quench cooled in air, ground, pelleted, and re-heated at 1400 ^oC for another two days. Diffraction patterns from the ceramics (brannerite and zirconolite) were collected using a PANalytical Empyrean X-ray diffractometer and a Co $K\alpha_{1,2}$ X-ray source at room temperature. Phase analysis was performed using the High Score Plus software package.[124]

Borosilicate glass (BG) and Fe-Al borosilicate glass (FABG) were synthesized by the ceramic method. The compositions of the borosilicate and Fe-Al borosilicate glasses are listed in Table 2.1. Appropriate amounts of the respective metal oxide powders were mixed, pressed into

pellets at 6 MPa and annealed at 1100 ºC for 1 hour in graphite crucibles. Labels used to name the glasses and glass-ceramic composites studied are listed in Table 2.2.

Table 2.1. Compositions of the synthesized glasses.

Glass	SiO_2 (mol %)	B_2O_3 (mol %)	Na_2O (mol %)	CaO (mol %)	Fe_2O_3 (mol %)	Al_2O_3 (mol %)
Borosilicate (BG)	63.5	16.9	16.5	3.1	-	-
Fe-Al borosilicate (FABG)	55.5	16.9	16.5	3.1	3.0	5.0

Table 2.2. Labels used to name the glasses and glass-ceramic composites studied.

Label	Sample description
BG	Borosilicate glass
FABG	Fe-Al-borosilicate glass
BG-$CeTi_2O_6$-750/1100 ºC	Composite materials containing brannerite in borosilicate glass annealed at either 750 or 1100 ºC
BG-$CaZrTi_2O_7$-750/1100 ºC	Composite materials containing zirconolite in borosilicate glass annealed at either 750 or 1100 ºC
BG-XX wt% $CeTi_2O_6$ or $CaZrTi_2O_7$	Composite materials containing XX wt% brannerite or zirconolite in borosilicate glass
FABG-XX wt% $CeTi_2O_6$ or $CaZrTi_2O_7$	Composite materials containing XX wt% brannerite or zirconolite in Fe-Al borosilicate glass

Glass-ceramic composite materials containing brannerite in borosilicate glass or Fe-Al borosilicate glass (BG/FABG-$CeTi_2O_6$) and zirconolite in borosilicate glass or Fe-Al borosilicate glass (BG/FABG-$CaZrTi_2O_7$) were synthesized by the ceramic method. The separately synthesized glass and ceramic materials were mixed and then annealed to form glass-ceramic composite materials. Different loadings of $CeTi_2O_6$ or $CaZrTi_2O_7$ (10 to 40 wt%) were mixed with appropriate amounts of borosilicate glass (BG) or Fe-Al-borosilicate glass (FABG) to form the glass-ceramic composites, pressed into pellets at 6 MPa, and then placed in graphite crucibles. The pellets were heated in air at 1100 or 750 ^oC for 1 hour. All composite materials were quench cooled in air and were observed to be beads after annealing at 1100 or 750 ^oC (see Figure 2.1). It has been reported previously that borosilicate glasses have softening and liquefication points above 800 and 1000 ^oC, respectively; however, these temperatures can be affected by the glass composition.[125,126]

The observation of both the glasses and glass-ceramic composites forming beads after annealing at 750 ^oC indicates that the glass compositions studied here had a liquid state at this temperature. The annealing temperatures used in this study were chosen so as to study how such significant differences in temperature impact the local and long-range structure of the composite materials.[17]

(a)  (b) 

Figure 2.1. Photographs of the composite material containing 30 wt% $CeTi_2O_6$ in borosilicate glass after annealing at (a) 750 or (b) 1100 ^oC are shown.

2.2.2. Electron microprobe analysis

The surface morphologies and chemical compositions of the samples were examined by collecting backscattered electron images (BSE) and energy dispersive X-ray (EDX) maps. BSE images and EDX maps were collected using a JEOL 8600 electron microprobe instrument. The glass-ceramic composite beads were embedded in a polymer resin and the surfaces of the beads were polished using diamond paste. The samples were coated with carbon to reduce charging effects.[17] BSE images were collected from the composite materials using a magnification of 1000X. Samples were mapped by EDX to determine the elemental distribution at different locations.

2.2.3. XANES

2.2.3.1. Ti K-, Zr K-, and Ce L_3-edges

Ti K-, Ce L_3- and Zr K-edge XANES spectra were collected using the Canadian Light Source/X-ray Science Division Collaborative Access Team (CLS@APS, Sector 20) bending magnetic beamline (20BM) located at the Advanced Photon Source (APS), Argonne National Laboratory.[127] A Si (111) double crystal monochromator with a harmonic rejection mirror was

used, which provides a photon flux of ~10^{11} photons/s.[127] The resolution of the spectra is 0.7 eV at 4966 eV (Ti K-edge), 0.9 eV at 5723 eV (Ce L_3-edge), and 2.6 eV at 17998 eV (Zr K-edge).[127] The samples were finely ground and sealed between layers of Kapton tape, and the thickness was adjusted by varying the number of layers of tape to maximize the absorption signal. Multiple scans of each spectrum were collected in fluorescence yield or transmission mode. The transmission spectra were recorded using ionization chambers filled with $He_{(g)}$ and $N_{2(g)}$ to achieve optimal absorption-edge step heights and signal-to-noise ratios.[128] The spectra were also collected in fluorescence mode using a single element vortex silicon detector. XANES spectra were collected using a step size of 0.15 eV/step through the Ti K- and Ce L_3-edges and 0.5 eV/step through the Zr K-edge.[129] The Ti K-edge spectra were calibrated using Ti metal (4966 eV) and the Ce L_3-edge spectra were calibrated using Cr metal (5989 eV).[17] The Zr K-edge spectra were calibrated using Zr foil as a reference standard with the absorption-edge energy set to 17998.0 eV.[129]

2.2.3.2. Fe K-edge

The Soft X-ray Microcharacterization Beamline (SXRMB, 06B1-1) located at the Canadian Light Source (CLS) was used to collect the Fe K-edge XANES spectra from Fe-Al borosilicate glass composite materials using a Si (111) monochromator.[130] This beamline provides a photon flux of 10^{11} photons/s and a resolution of 0.7 eV at 7112 eV.[130] The powdered samples were sealed between layers of Kapton tape and the spectra were collected in fluorescence yield and transmission modes using a step size of 0.15 eV through the Fe K-edge. The spectra were calibrated using Fe foil (7112 eV).[130]

2.2.3.3. Si and Al $L_{2,3}$-edges

The Si and Al $L_{2,3}$-edge XANES spectra were collected from the composite materials using the Variable Line Spacing-Plane Grating Monochromator (VLS-PGM) beamline at the CLS.[131]

The samples were prepared by placing ground powder on carbon tape. The spectra were collected in total fluorescence yield (TFY) mode using a step size of 0.05 eV through the Si and Al $L_{2,3}$-edges. The spectra were calibrated using elemental Si for the Si $L_{2,3}$-edge (99.4 eV) and Al metal for the Al $L_{2,3}$-edge (72.5 eV).[17,131] All XANES spectra were normalized and analyzed using the Athena software program.[132]

2.3. Results and discussion

2.3.1. Powder X-ray diffraction

Powder XRD patterns from the glass-ceramic composite materials were collected from powdered samples to obtain information about the long-range structure of these materials. The XRD patterns from the glasses (BG and FABG) annealed at different temperatures are shown in Figures 2.2a and 2.2b. Unique powder patterns were observed depending on if the glass-ceramic composite materials were annealed at 750 ^{o}C or 1100 ^{o}C, as has been observed previously.[17] The patterns from the glasses annealed at 1100 ^{o}C (BG-1100 ^{o}C and FABG-1100 ^{o}C) show only a broad hump which confirms the amorphous structure of these materials. However, the diffraction pattern from the borosilicate glass annealed at 750 ^{o}C contains peaks that correspond to the presence of quartz (SiO_2), whereas no such peaks were observed in the XRD pattern from the Fe-Al borosilicate glass annealed at 750 ^{o}C. The stabilization of the amorphous structure of the Fe-Al borosilicate glass sample was assumed to be a result of the presence of Al.[17] It was shown previously that Al is responsible for stabilizing the amorphous structure of the Fe-Al-borosilicate glass.[17,133] Aluminum is a network intermediate and can behave as a network former or a network modifier.[17,133-135] Al is known to substitute into 4- to 6- coordinate positions, potentially leading to disordering of the quartz and a stabilization of the amorphous structure of the glass.[134-136]

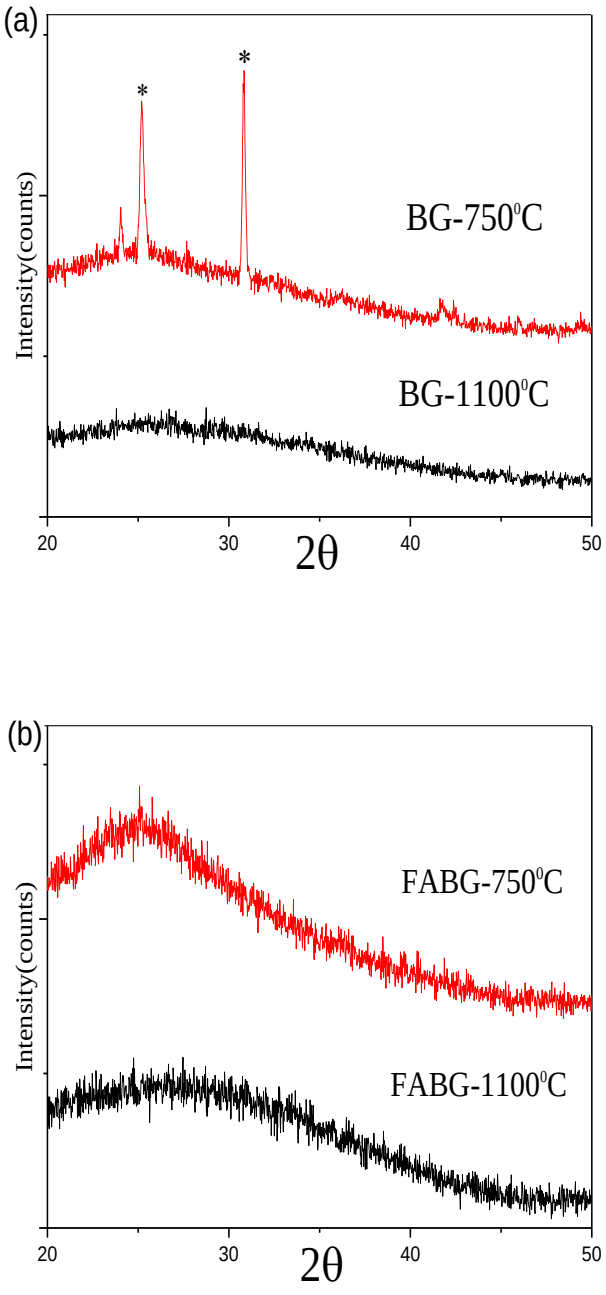

Figure 2.2. XRD patterns from (a) borosilicate glass annealed at 750 or 1100 °C and (b) Fe-Al borosilicate glass annealed at 750 or 1100 °C are shown. Diffraction peaks from quartz are marked by an asterisk (*).

Powder XRD patterns were collected from composite materials containing different amounts of $CeTi_2O_6$ in borosilicate glass annealed at 750 or 1100 ^oC (Figures 2.3a and 2.3b). Diffraction patterns from the BG-$CeTi_2O_6$ composites annealed at 750 ^oC contain peaks from $CeTi_2O_6$ and quartz, as well as a broad hump that is representative of the amorphous glass matrix. The patterns from the composite materials annealed at 1100 ^oC (Figures 2.3b) shows that peaks from brannerite only started to remain in diffraction patterns of the composite materials when 40 wt% of $CeTi_2O_6$ was loaded in the glass matrix. These observations indicate that a significant amount of the brannerite crystallites dissolved in the glass matrix after annealing at 1100 ^oC.

XRD patterns were also collected from the BG-$CaZrTi_2O_7$ composite materials containing different amounts of $CaZrTi_2O_7$ annealed at 750 or 1100 ^oC (Figures 2.4a and 2.4b). Examination of the patterns from the composite materials annealed at 1100 ^oC showed that the minimum loading of $CaZrTi_2O_7$ when peaks representing zirconolite started to appear in the diffraction patterns was 40 wt% (Figure 2.4b). Diffraction peaks from zirconolite were observed in all patterns from BG-$CaZrTi_2O_7$ annealed at 750 ^oC regardless of loading (Figure 2.4a); however, peaks representing the presence of quartz were not observed. The lack of peaks corresponding to the presence of quartz is likely a result of Ca from zirconolite that had dissolved in the glass matrix, acting as a network modifier.[5,87,88,135] These results suggest that a low annealing temperature (i.e., 750 ^oC) is more favourable to the formation of a composite material with a negligible amount of the ceramic having dissolved in the glass matrix.

XRD patterns from Fe-Al borosilicate glass composite materials containing brannerite or zirconolite annealed at either 750 or 1100 ^oC are shown in Figures A1.1 and A1.2 in Appendix A1. Diffraction patterns from these composite materials were observed to be similar to the patterns from borosilicate glass-based composite materials. These results indicate that the type of glass

used (i.e., borosilicate or Fe-Al borosilicate) does not influence how the annealing temperature affected the average structure of these composite materials.

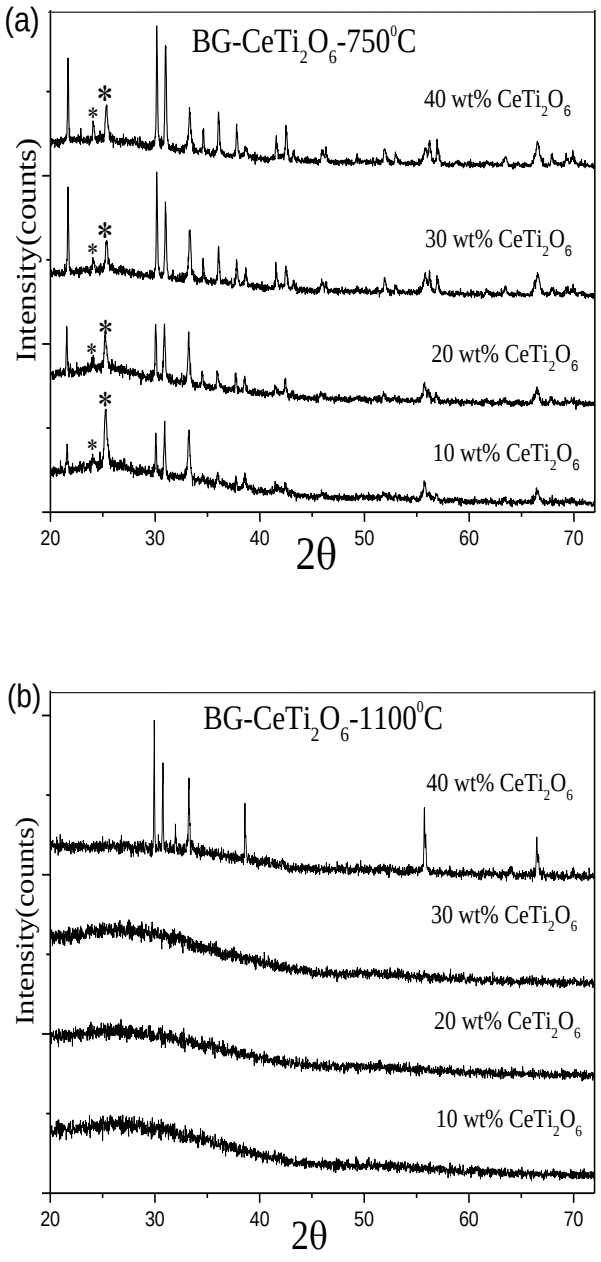

Figure 2.3. XRD patterns from the powdered composite materials containing 10, 20, 30 and 40 wt% loading of $CeTi_2O_6$ in borosilicate glass annealed at (a) 750 or (b) 1100 ^oC are shown. Diffraction peaks from quartz are marked by an asterisk (*).

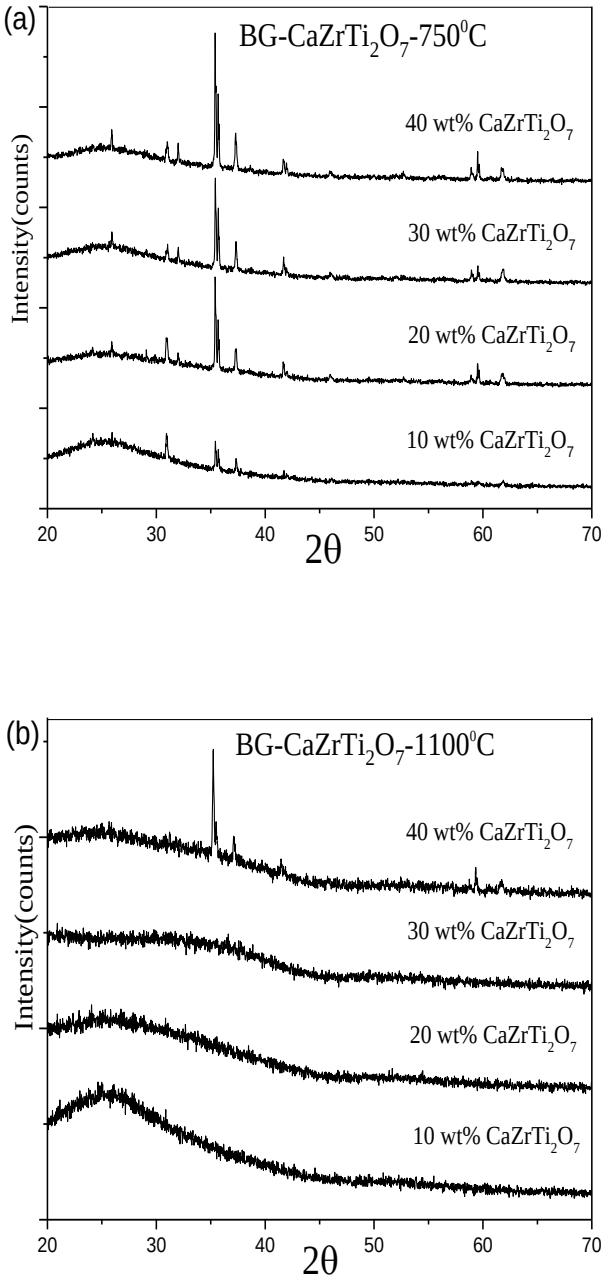

Figure 2.4. XRD patterns from the powdered composite materials containing 10, 20, 30 and 40 wt% loading of $CaZrTi_2O_7$ in borosilicate glass annealed at (a) 750 or (b) 1100 ^oC are shown.

2.3.2. Electron microscopy and EDX

BSE images from the borosilicate glass composite materials (BG-$CeTi_2O_6$/$CaZrTi_2O_7$) annealed at either 750 or 1100 ^oC are shown in Figure 2.5. The BSE images from the glass-ceramic composite materials (see Figure 2.5) show that the brannerite or zirconolite crystallites (bright area) can be differentiated from the glass matrix (dark area). Air bubbles formed during annealing were also observed in the images from these materials.

The BSE images from the composite materials annealed at 1100 ^oC (Figures 2.5b and 2.5d) contained smaller crystallites when compared to the images from the composite materials annealed at 750 ^oC (Figures 2.5a and 2.5c). Examination of EDX maps (see Figures A1.3 and A1.4 in Appendix A1) from the composite materials containing brannerite annealed at 1100 ^oC shows that the glass-like regions contained high concentrations of Ce and Ti (Figure A1.4). The presence of Ce and Ti was observed only in the ceramic crystallites when an annealing temperature of 750 ^oC was used to form the glass-ceramic composite materials (Figure A1.3). These results confirm that more brannerite/zirconolite crystallites dissolved in the glass matrix after annealing at higher temperatures (i.e., 1100 vs 750 ^oC). These observations are in good agreement with the analysis of the XRD patterns (*vide supra*).

2.3.3. XANES analysis

Examination of Ti K-, Ce L_3-, Zr K-, Si $L_{2,3}$-, Fe K-, and Al $L_{2,3}$-edge XANES spectra from the glass-ceramic composite materials has allowed for a study of how the annealing temperature, glass composition, and the loading of the ceramic crystallites affected the local environment of the glass-ceramic composites.

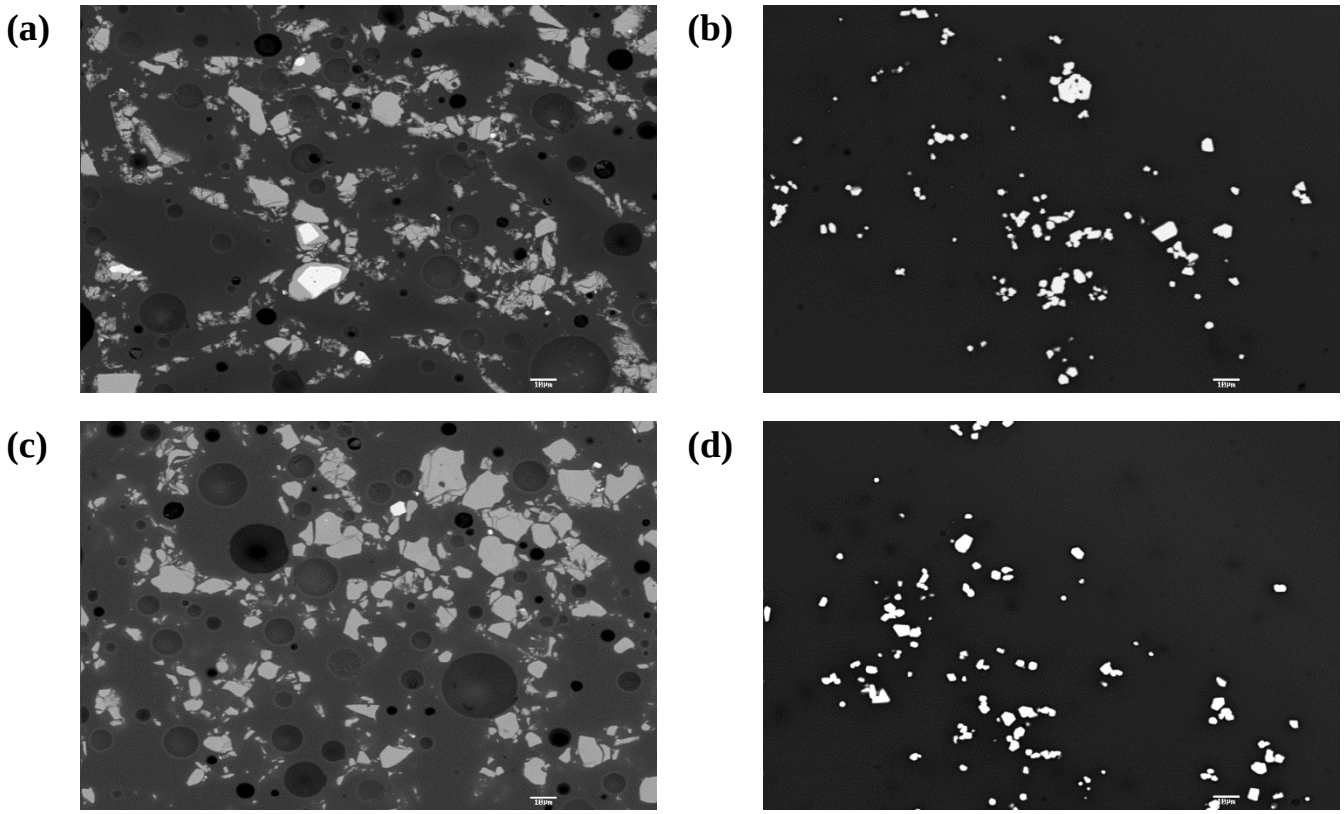

Figure 2.5. Backscattered images from (a) BG-30 wt% $CeTi_2O_6$-750 ^oC, (b) BG-30 wt% $CeTi_2O_6$-1100 ^oC, (c) BG-30 wt% $CaZrTi_2O_7$-750 ^oC, and (d) BG-30 wt% $CaZrTi_2O_7$-1100 ^oC are shown. The scale bar in each image is 10 μm. Backscattered images were collected from polished composite beads.

2.3.3.1. Ti K-edge XANES

Ti K-edge XANES spectra were collected from the BG-$CeTi_2O_6$ and BG-$CaZrTi_2O_7$ composite materials containing 10, 20, and 30 wt% of $CeTi_2O_6$ or $CaZrTi_2O_7$ annealed at either 750 or 1100 ^oC (see Figures 2.6 and 2.7). Examination of the Ti K-edge spectra shows how the loading of the ceramic ($CeTi_2O_6$ or $CaZrTi_2O_7$) in the glass matrix and the annealing temperature used can affect the local coordination environment of Ti in the composite materials. These spectra result from 1s→3d (electric quadrapolar; pre-edge (A)) and 1s→4p (electric dipolar; main-edge (B and C)) transitions.[17,83,137] The pre-edge region (features A_1, A_2 and A_3) contains peaks resulting from local 1s→3d t_{2g} (A_1) and 1s→3d e_g^* (A_2) transitions, as well as a third peak (A_3) that results

from a non-local, intersite-hybrid excitation involving the transition of 1s electrons to unoccupied 3d orbitals from a next-nearest-neighbour Ti ion that overlaps with 4p orbitals from the absorbing Ti ion through bridging O 2p orbitals.[17,83,137,138]

The intensity of the pre-edge feature (A) increases while the energy (B) and intensity (C) of the main-edge features decrease with decreasing Ti coordination number (CN).[118,138-141] The quadrupolar transition (pre-edge (A)) is normally forbidden by dipole selection rules but it becomes allowed with mixing of d and p orbitals.[17,83,118,138-141] An increase in the intensity of the pre-edge peak is observed for a site without a centre of symmetry (i.e., TiO_4 tetrahedron or a TiO_5 square pyramid) because of the mixing 3d with 4p orbitals, which provides some dipole allowed character to the quadrupolar transition. The pre-edge peak can therefore be used to infer the Ti CN.[17,83,138-141] The energy and intensity of the main-edge features (B and C) can change because of variations in CN and/or oxidation state.[123,137] Feature B can shift to a lower energy because of a decrease in CN.[138,139] A lower CN results in greater final state relaxation effects due to the presence of fewer electrons in the first coordination-shell leading to a shift down in absorption energy.[138] The intensity of feature C is also affected by changes in the CN. As the CN decreases, this reduces the number of Ti 4p-2p O final states available for 1s electrons to be excited to, resulting in a decrease in the intensity of feature C.[138] Feature B (and C) can also shift in energy with changing oxidation state. An increase in the oxidation state will result in fewer electrons being available to screen the nuclear charge and, therefore, more energy is required to excite core electrons leading to an increase in the observed absorption energy.[17,123,137]

Examination of the Ti K-edge spectra from the BG-$CeTi_2O_6$ composite materials annealed at either 750 (Figure 2.6a) or 1100 ^oC (Figure 2.6b) shows that the intensity and energy of the pre-edge and main-edge features changed by varying the loading of brannerite in the glass matrix or

by varying the annealing temperature used to form these composite materials. It was observed that the intensity of the pre-edge feature (A) increased while the energy (B) and intensity (C) of the main-edge features decreased with increasing annealing temperature or decreasing brannerite loading in the composite materials when compared to the spectrum from $CeTi_2O_6$ (see Figures 2.6a and 2.6b). These changes in the Ti K-edge XANES spectra were attributed to a decrease in the CN of Ti^{4+}.[118,138-141] It is recognized that the shift down in energy of feature B could also suggest that Ti^{4+} is reduced in the composite materials, however a reduction in the Ti oxidation should also lead to a decrease in the intensity of the pre-edge peak (feature A) which was not observed. The observed increase in the intensity of feature A and decrease in energy of feature B when comparing the composite materials to $CeTi_2O_6$ can only be attributed to a lowering of the average Ti CN.[17,83,118,138-141] Titanium adopts a lower CN when incorporated in the glass versus when it is incorporated in brannerite.[17] Moreover, the average Ti CN is lower in the BG-$CeTi_2O_6$ composites annealed at 1100 ^oC compared to the composites annealed at 750 ^oC, further confirming that more brannerite dissolved in the glass matrix after annealing at 1100 ^oC.

Ti K-edge XANES spectra from the BG-$CaZrTi_2O_7$ composite materials annealed at either 750 or 1100 ^oC are shown in Figures 2.7a and 2.7b. The intensity of the pre-edge feature (A) increased with increasing annealing temperature or decreasing zirconolite loading in the composite materials when compared to the spectrum from $CaZrTi_2O_7$ (see Figures 2.7a and 2.7b).

These observations indicate that Ti occupies a lower CN when incorporated in the glass than in the ceramic.[17] The composite materials containing zirconolite annealed at 1100 ^oC show a lower Ti CN compared to the composite materials annealed at 750 ^oC because more zirconolite dissolved in the glass after annealing at 1100 ^oC. The comparison of the Ti K-edge spectra from the composite materials containing brannerite or zirconolite crystallites show that similar changes

in the coordination environment of Ti occur when the synthesis conditions were changed. These observations show that the local structure of Ti in the glass-ceramic composite materials is affected strongly by the annealing temperature, which agrees with the powder XRD and electron microscopy results discussed above.

Ti K-edge spectra were also collected from the composite materials containing 30 wt% $CeTi_2O_6$ and 30 wt% $CaZrTi_2O_7$ in Fe-Al borosilicate glass annealed at either 750 or 1100 ^oC to determine if the type of glass used affects the local coordination environment of Ti in these composite materials (see Figures A1.5 and A1.6 in Appendix A1). Comparing the spectra from the BG-30 wt% $CeTi_2O_6$ and FABG-30 wt% $CeTi_2O_6$ composites annealed at either 750 (Figure A1.5a) or 1100 ^oC (Figure A1.5b) shows that the type of glass used does not affect the behaviour of Ti in these glass-ceramic composite materials. Comparison of the spectra from BG and FABG composite materials containing 30 wt% $CaZrTi_2O_7$ annealed at either 750 (Figure A1.6a) or 1100 ^oC (Figure A1.6b) also shows that the behaviour of Ti is not affected by changing the type of glass used to form these composite materials.

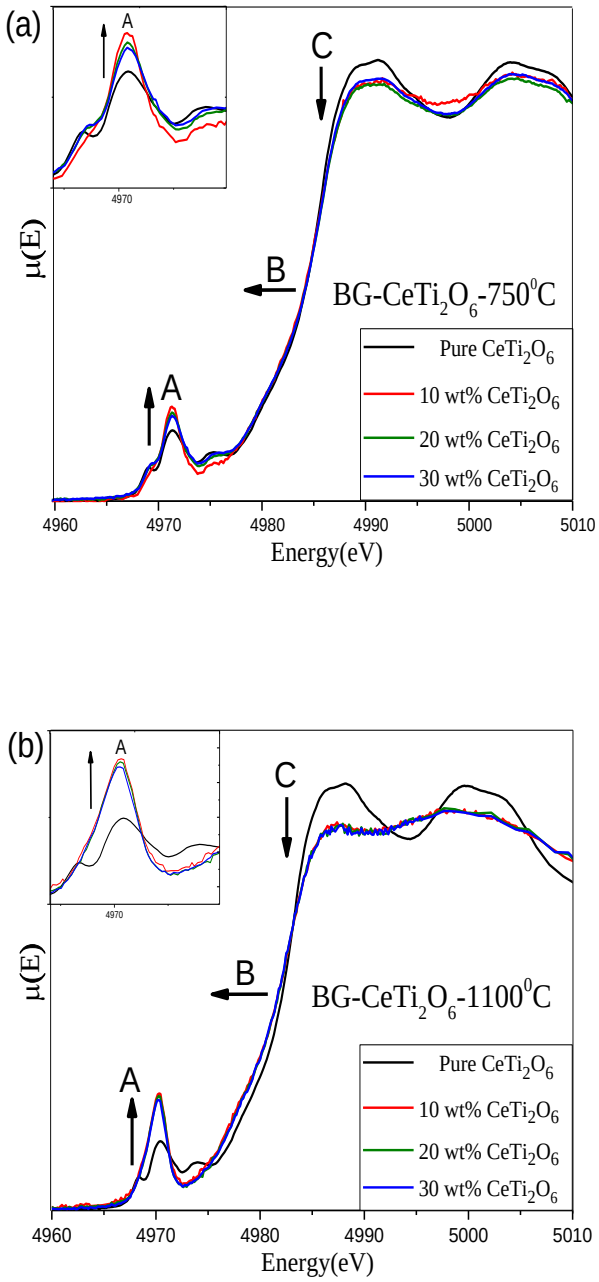

Figure 2.6. Ti K-edge XANES spectra from (a) BG-$CeTi_2O_6$-750 ^oC and (b) BG-$CeTi_2O_6$-1100 ^oC containing 10, 20 and 30 wt% loading of $CeTi_2O_6$ are shown. The spectrum from $CeTi_2O_6$ is also presented. Feature A represents the pre-edge region (1s→3d) and is shown in the inset. Features B and C (1s→4p) represent the main-edge region. The arrows show how the intensity or energy of the spectral features change with decreasing loading of the ceramic in the glass-ceramic composites when compared to the spectrum from $CeTi_2O_6$.

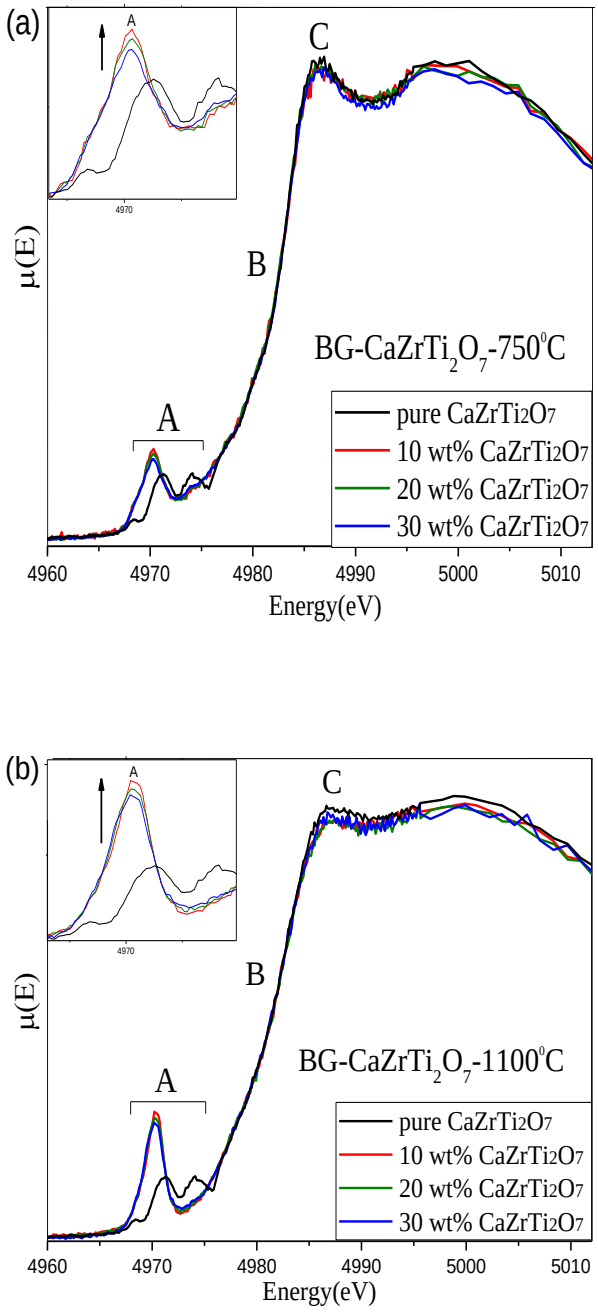

Figure 2.7. Ti K-edge XANES spectra from (a) BG-$CaZrTi_2O_7$-750 ^oC and (b) BG-$CaZrTi_2O_7$-1100 ^oC containing 10, 20 and 30 wt% loading of $CaZrTi_2O_7$. The spectrum from $CaZrTi_2O_7$ is also presented. Feature A (pre-edge region) is shown in the inset. The arrows show how the intensity of the pre-edge feature (A) increased with decreasing loading of the ceramic in the glass-ceramic composites when compared to the spectrum from $CaZrTi_2O_7$.

2.3.3.2. Ce L_3-edge XANES

Ce L_3-edge XANES spectra were collected from the BG-$CeTi_2O_6$ composite materials annealed at either 750 or 1100 ^oC to study how the local environment of Ce changes in these materials and are shown in Figure 2.8. Four features are observed in these spectra from Ce^{4+}, which are labelled as B_1, B_2, B_3, and B_4 (see Fig. 2.8). The spectra result from a quadrupolar 2p $\rightarrow$4f transition (B_1) and three dipolar 2p $\rightarrow$5d transitions where the final-states of Ce changes to $4f^2$ (B_2), $4f^1$ (B_3), and $4f^0$ (B_4).[83,142]

Examination of the Ce L_3-edge XANES spectra from the BG-$CeTi_2O_6$ composite materials shows that the intensity and energy of the pre-edge and main-edge features changed when the annealing temperature was changed from 750 to 1100 ^oC. The observed changes in the Ce L_3-edge spectra from the composite materials are a result of a variation in the Ce oxidation state.[142,143] The presence of features B_3 and B_4 are indicative of Ce^{4+} while the observation of an intense B_2 peak is indicative of the presence of Ce^{3+}.[83,142,143] Comparing the intensity of features B_2 , B_3 and B_4 in the spectra shows that the average Ce oxidation state is lower in the composite materials annealed at 1100 ^oC versus the composite materials annealed at 750 ^oC. The changes in the Ce oxidation state can be attributed to a temperature-dependant equilibrium between O and Ce ($4Ce^{4+}+2O^{2-} \rightleftharpoons 4Ce^{3+}+O_2$).[83,142,143] As the annealing temperature of the system increases, the equilibrium shifts towards the reduced state of Ce (i.e., Ce^{3+}).[83,142,143] This effect was observed to be greater when Ce was contained in the glass matrix compared to when it was contained in the ceramic ($CeTi_2O_6$) as a result of brannerite dissolving in the glass matrix when an annealing temperature of 1100 ^oC was used.[83] The major oxidation state of Ce was observed to be 4+ for all composite materials annealed at 750 ^oC while the presence of Ce^{3+} increased with decreasing loading of brannerite in the BG-$CeTi_2O_6$ composite materials annealed at 1100 ^oC. This observation confirms that brannerite

dissolved in the glass matrix when the composite materials were annealed at 1100 ^{o}C but only up to a certain loading (30-40 wt%), after which some crystalline brannerite was observed to be present.

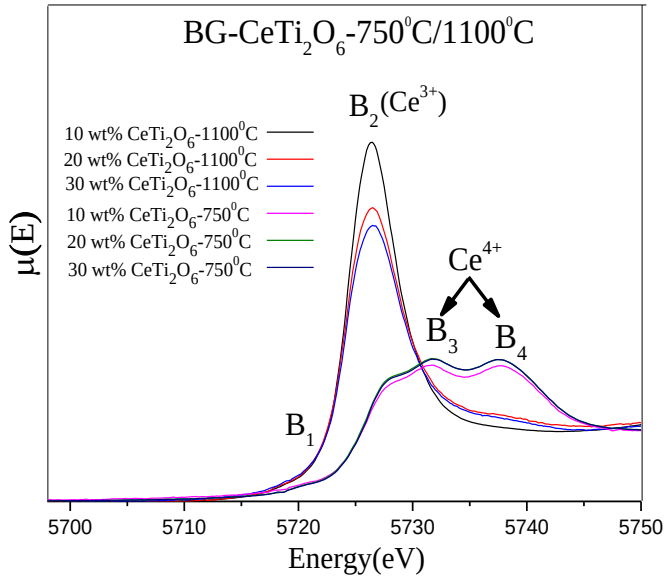

Figure 2.8. Ce L_3-edge XANES spectra from BG-$CeTi_2O_6$ composite materials containing 10, 20 and 30 wt% loading of $CeTi_2O_6$ annealed at 750 or 1100 ^{o}C are shown.

2.3.3.3. Zr K-edge XANES

Zr K-edge spectra were collected from the composite materials containing $CaZrTi_2O_7$ in order to understand how the Zr CN in the BG-$CaZrTi_2O_7$ composites was affected by the synthesis conditions used to form these materials (Figure 2.9). A distinct pre-edge peak (1s→4d) is not observed in the Zr K-edge XANES spectra because of the low resolution of the spectra and the decreased separation between Zr 4d and 5p orbitals when compared to first row transition metals like Ti.[144,145] Although the resolution of the pre-edge peak in the Zr K-edge spectra makes it difficult to investigate changes in Zr CN, the main-edge features are sensitive to CN changes.[144,145]

The spectrum from zirconolite exhibited a broad maximum in the main edge at around 18017 eV, which is in good agreement with previous studies of materials containing 7-coordinate Zr ($Zr^{[7]}$).[144-147] The intensity, energy, and lineshape of the pre-edge and main-edge features of the spectra were observed to change as the annealing temperature of the composite materials was varied. The observed changes in the Zr K-edge XANES spectra (i.e., large differences in the spectral lineshape) have been shown previously to result from variations in the CN of Zr^{4+}.[144-147] A double peak in the main edge with a maximum around 18030 eV is observed in the Zr K-edge XANES spectra from materials containing six-coordinate Zr while a single broad peak in the main edge is observed for materials containing seven-coordinate Zr.[144-147] These observations fit well with the observations of Zr K-edge XANES spectra from the composite materials presented here and indicate that Zr adopts a lower CN when it is incorporated in the glass matrix than in zirconolite crystallites.[148] Moreover, comparing the Zr K-edge XANES spectra from the glass-ceramic composite materials shows that the average Zr CN is lower in the composites annealed at 1100 ^{o}C compared to the composite materials annealed at 750 ^{o}C. As the annealing temperature increased, the CN of Zr decreased in the composites because of zirconolite crystallites dissolving in the glass matrix.

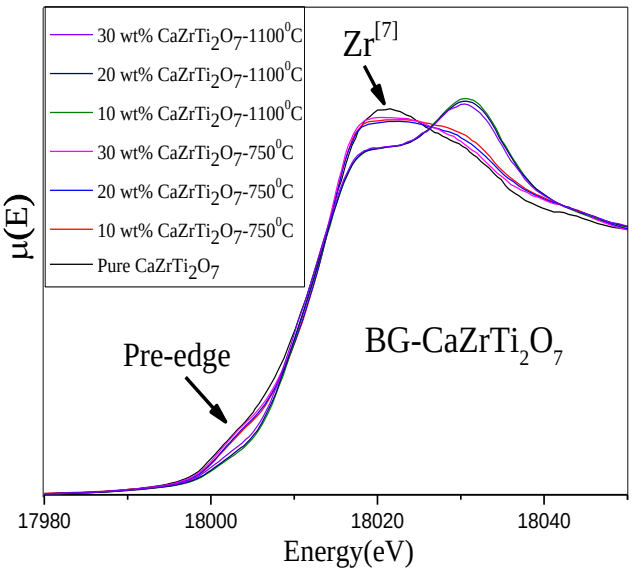

Figure 2.9. Zr K-edge XANES spectra from BG-$CaZrTi_2O_7$ composite materials containing 10, 20 and 30 wt% loading of $CaZrTi_2O_7$ annealed at 750 or 1100 ^oC are shown. The spectrum from $CaZrTi_2O_7$ is also presented for comparison.

2.3.3.4. Si $L_{2,3}$-edge XANES

Si $L_{2,3}$-edge XANES spectra were collected to study how the local structure of Si in the glass was affected by varying the loading of the ceramic, annealing temperature, and the type of glass used to form the composite materials. The Si $L_{2,3}$-edge XANES spectra contain two features that result from 2p→3s (Feature D) and 2p→3d (Feature E) transitions, respectively. The low-energy feature (D) is split into two peaks (D_1 and D_2) due to spin-orbit splitting.[149,150]

It was observed in previous studies of Si $L_{2,3}$ edge XANES spectra that features D and E become narrower to higher energy on going from amorphous silicate to quartz.[17,150-152] The spectra from materials containing amorphous silicates (i.e. glass) have broader peaks to lower energy compared to their crystalline analogues, which can be attributed to the lack of long range order in

amorphous silicates.[150-152] As the materials change from amorphous silicates to quartz, a more ordered SiO_4^{4-} tetrahedral bond network would be present, leading to an increase in the degeneracy of Si-O conduction states. This effect results in features D and E becoming narrower to higher energy.[17,150-152]

The Si $L_{2,3}$-edge XANES spectra from the composite materials containing different amounts of $CeTi_2O_6$ or $CaZrTi_2O_7$ in the glass (BG and FABG), and annealed at different temperatures are shown in Figures 2.10, 2.11 and A1.7. The spectra from the corresponding glasses (BG or FABG) are also presented in these figures. The width of the spectral features (D, E) from the composite materials were observed to decrease with increasing loading of the ceramic, decreasing the annealing temperature, or varying the type of glass used to form these materials (i.e., BG vs FABG). The observed changes in the spectra can be attributed to changes in the ordering of the glass in the composites as a result of the partial crystallization of the glass matrix and variations in the glass composition as a result of ceramic crystallites dissolving in the glass network leading to next nearest-neighbour effects between the metal cations and Si.[17,150-153] The next nearest-neighbour metal cation (M) in the Si-O-M bond can influence the strength, length, and bonding characteristics of the Si-O bond.[150-153] The observed changes in the Si $L_{2,3}$ edge XANES spectra from the composite materials indicate that the variation in the loading of $CeTi_2O_6$ or $CaZrTi_2O_7$, the annealing temperature, and the glass composition affect the silicate network. The Si $L_{2,3}$-edge spectra from the BG-composite materials showed more changes when compared to the spectra from the FABG-composite materials. These observations indicate that the silicate environment in the borosilicate glass matrix is affected to a greater degree than in the Fe-Al borosilicate glass matrix because of the partial crystallization of the borosilicate glass and next nearest-neighbour effects due to the variation in the glass composition.[17] Moreover, features D and

E in the spectra from BG-$CeTi_2O_6$-750 ^oC were observed to be sharper when compared to the spectra from BG-$CaZrTi_2O_7$-750 ^oC. This observation can be attributed to the presence of quartz in the borosilicate glass composite materials containing $CeTi_2O_6$ annealed at 750 ^oC, as quartz was not detected to be present in the BG-$CaZrTi_2O_7$-750 ^oC analogues by XRD.

2.3.3.5. Fe K-edge XANES

Fe K-edge XANES spectra were collected to study how the redox chemistry of Fe in the Fe-Al borosilicate glass matrix can affect the local structure of the composite materials. The Fe K-edge XANES spectra contain pre-edge (1s→3d, A) and main-edge (1s→4p, B and C) excitations that resemble the features observed in Ti K-edge XANES spectra.[154-156] The Fe K-edge spectra from the composite materials (FABG-30 wt% $CeTi_2O_6$ and FABG-30 wt% $CaZrTi_2O_7$) annealed at 750 or 1100 ^oC are shown in Figures 2.12a and 2.12b.

The Fe K-edge spectra from the composite materials containing 30 wt% $CeTi_2O_6$ or $CaZrTi_2O_7$ in Fe-Al borosilicate glass showed a significant shift of the main edge (feature B) to lower energy along with a decrease in the pre-edge peak intensity (feature A) in the composite materials annealed at 1100 ^oC versus those annealed at 750 ^oC. The observed decrease in the intensity of feature A and energy of feature B can only be attributed to a variation in Fe oxidation state based on the reasons provided above when discussing the Ti K-edge XANES spectra (Section 2.3.3.1). The Fe K-edge XANES spectra indicate that the oxidation state of Fe in the composite materials annealed at 1100 ^oC was reduced to 2+ while the oxidation state of Fe in the composite materials annealed at 750 ^oC was 3+.[157-159] The observed change in Fe oxidation state with varying annealing temperature is a result of a redox reaction and a temperature-dependant equilibrium between O and Fe ($4Fe^{3+}+2O^{2-} \rightleftharpoons 4Fe^{2+}+O_2$). The equilibrium shifts towards Fe^{2+} when the annealing temperature increases.[17,157]

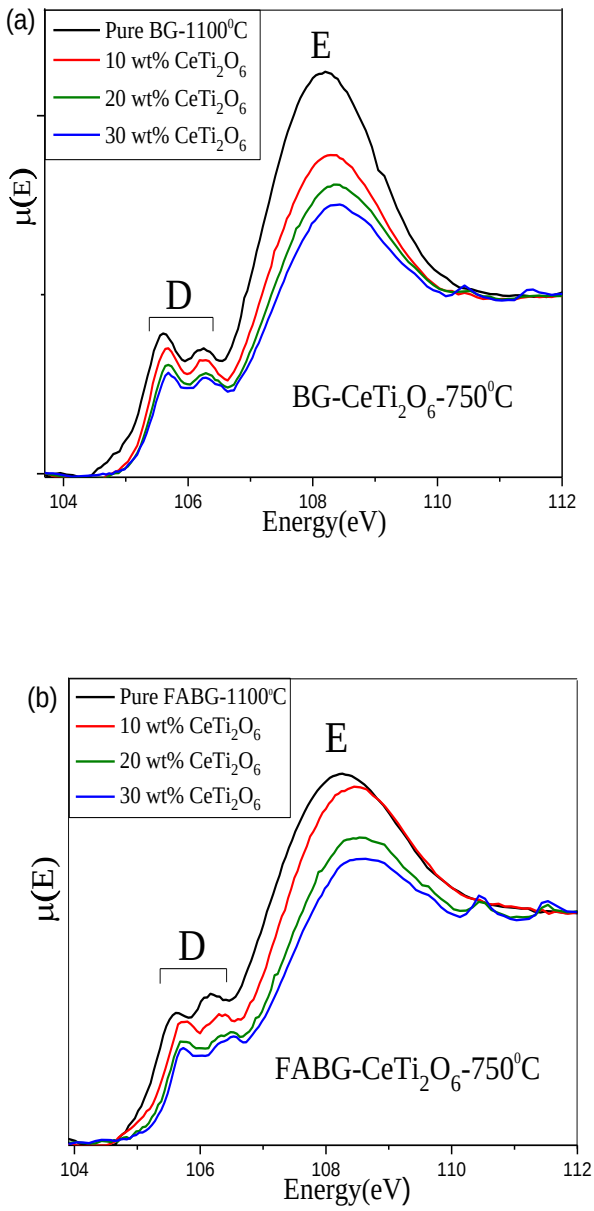

Figure 2.10. Si $L_{2,3}$-edge XANES spectra from (a) BG-$CeTi_2O_6$-750 ºC and (b) FABG-$CeTi_2O_6$-750 ºC containing 10, 20 and 30 wt% loading of $CeTi_2O_6$ are shown. The spectra are compared to the spectrum from the corresponding glass (BG or FABG).

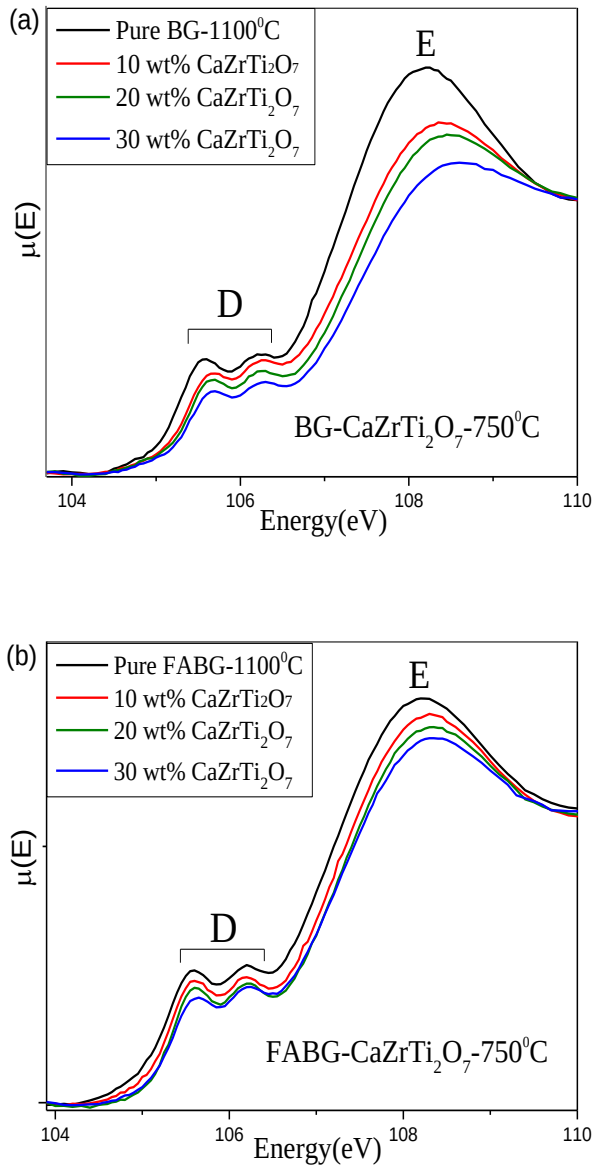

Figure 2.11. Si $L_{2,3}$-edge XANES spectra from (a) BG-$CaZrTi_2O_7$-750 ^oC and (b) FABG-$CaZrTi_2O_7$- 750 ^oC containing 10, 20 and 30 wt% loading of $CaZrTi_2O_7$ are shown. The spectra are compared to the spectrum from the corresponding glass (BG or FABG).

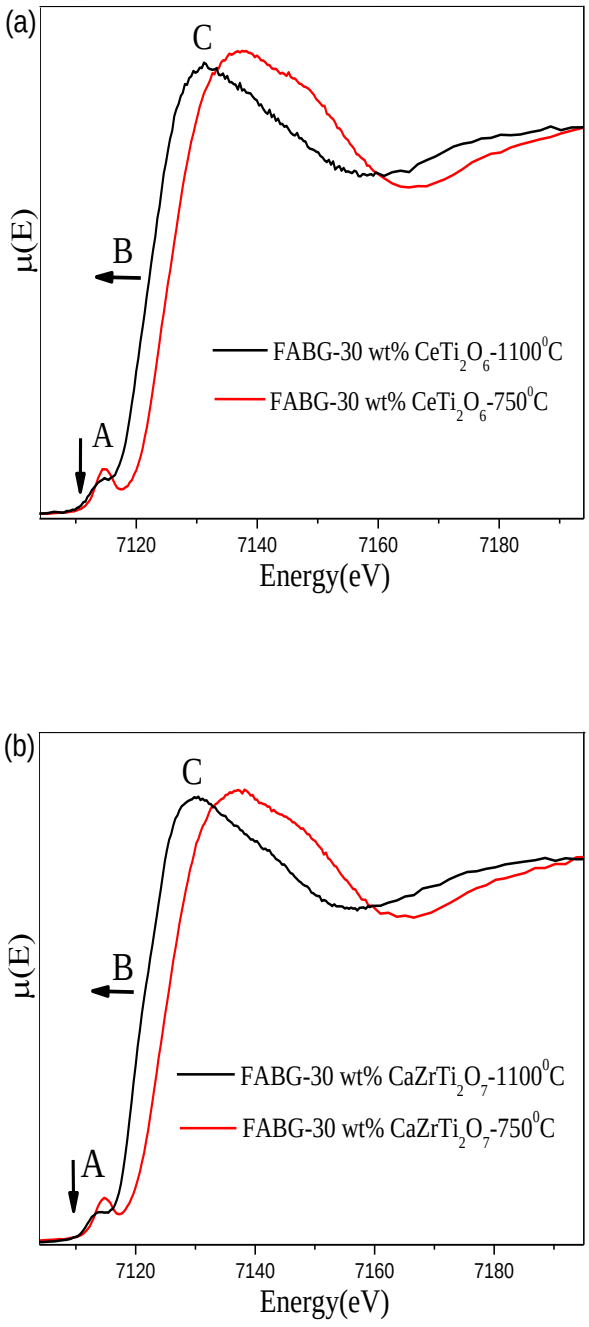

Figure 2.12. Fe K-edge XANES spectra from (a) FABG-30 wt% $CeTi_2O_6$ -750 or 1100 ºC, and (b) FABG-30 wt% $CaZrTi_2O_7$-750 or 1100 ºC. The spectra result from 1s→3d (feature A) and 1s→4p (Features B and C) transitions, respectively. The arrows show a shift of the main edge (feature B) to lower energy along with a decrease in the pre-edge peak intensity (feature A) in the composite materials annealed at 1100 ºC versus those annealed at 750 ºC.

2.3.3.6. Al $L_{2,3}$-edge XANES

Al $L_{2,3}$-edge XANES spectra were collected from the FABG-$CeTi_2O_6$ composite materials annealed at either 750 or 1100 ^oC to study the local environment of Al (see Figure A1.8 in supporting information). The spectra contain two features (D and E) that result from 2p→3s and 2p→3d transitions, respectively.[160] It has been shown previously that Al $L_{2,3}$-edge XANES spectra are sensitive to changes in the CN of Al.[160] In the present work, examination of the spectra from the composite materials show negligible changes in the spectral features. These observations indicate that the local structure of Al in the composite materials is not affected considerably by varying the loading of the ceramic or the annealing temperature used to form these composite materials.

2.4. Conclusions

A good insight into the local structure of glass-ceramic composite materials has been achieved by the investigation of borosilicate and Fe-Al-borosilicate glass-ceramic composites containing brannerite or zirconolite crystallites. These investigations have shown that the $CeTi_2O_6$ or $CaZrTi_2O_7$ crystallites can dissolve in the glass matrix depending on the ceramic loading, the glass composition, and the annealing temperature used to form these composite materials. It was observed that the $CeTi_2O_6$ or $CaZrTi_2O_7$ crystallites can dissolve significantly in the glass matrix when annealed at high temperature. Examination of Ti K- and Zr K-edge XANES spectra from the composite materials indicated that applying a lower annealing temperature is desired for the formation of a composite material with only a small fraction of the ceramic crystallites ($CeTi_2O_6$ or $CaZrTi_2O_7$) having dissolved in the glass matrix. The Si $L_{2,3}$-edge XANES spectra showed that the ordering of the silicate network can be affected depending upon the loading of $CeTi_2O_6$ or $CaZrTi_2O_7$, annealing temperature, and the type of glass used to form these composite materials.

Further, the study of the Ce L_3- and Fe K-edge XANES spectra from the Fe-Al-borosilicate composites showed that the oxidation state of Ce and Fe in the glass-ceramic composite materials is strongly affected by the annealing temperature. The comparison of glass-ceramic composite materials containing brannerite and zirconolite has shown that similar changes in the long-range and local structure of these composite materials occurs as a result of changing the synthesis conditions. The study of these composite materials will provide a better understanding of how to design materials with considering synthesis conditions for sequestration application as well as for other applications.

Chapter 3

Investigation of the stability of glass-ceramic composites containing $CeTi_2O_6$ and $CaZrTi_2O_7$ after ion implantation

3.1. Introduction

Glass and ceramic materials have been examined for nuclear waste sequestration applications in the past.[5,29,34,51-55,62-67,72-77,83] Glass wasteforms exhibit varying degrees of resistance to radiation induced structural damage depending on glass composition.[5,8,34,54,55] Previous investigations of borosilicate glasses have shown that the glass composition affects the resistance of these materials to radiation damage.[5,8,34,54,55] Ion beam implantation studies of $RE_2Zr_2O_7$ and $RE_2Ti_2O_7$ (RE=La–Lu, Y) crystallites have shown the importance of the structure of the ceramic (i.e., A- and B-site ionic radius) to the resistance of these materials to radiation induced structural damage.[29,34,72-77,80-83,87,88] However, few studies have investigated the effect of radiation induced structural damage depending on the composition of glass-ceramic composite materials.[4-10,17,27,34] A previous study of ion implanted glass-ceramic composite materials containing pyrochlore-type ceramics showed that the damage experienced by pyrochlore-type oxides ($Gd_2Ti_2O_7$) in the composite materials was similar to the pure ceramic (i.e., $Gd_2Ti_2O_7$).[17]

Investigating the long-term radiation damage of a wasteform is not possible on a real time scale (i.e., 10^3-10^6 years) but radiation induced structural damage can be simulated by bombarding (implanting) materials using high-energy ion beams (e.g., Au^-, Kr^+, Xe^+ and etc).[56-61,95-97] Ion implantation produces an amorphous layer which is typically only a few hundred nm thick.[17,56,89,96,99] Glancing angle XANES (GA-XANES) can be used to probe the amorphous (damaged) surface layer of a material produced by ion implantation.[17,89,121-123] During a

GA-XANES experiment, the incident X-ray beam angle is set to be just above the critical angle (the angle at which total external reflection occurs) to selectively probe the damaged surface layer of a material.[17,89,121-123] The objective of this study was to investigate how radioactive decay of incorporated nuclear waste elements can affect the structural stability of a glass-ceramic composite wasteform.

In this study, glass-ceramic composite materials containing brannerite or zirconolite in borosilicate glass were implanted by 2 MeV Au^- ions to a dose of 5×10^{14} ions/cm^2 at room temperature to investigate how the structure of these glass-ceramic composite wasteforms can resist structural damage caused by incorporated nuclear waste elements. The objective of this study was to understand how the structure of a composite wasteform responds to the radioactive decay of incorporated nuclear waste elements. A combination of ion implantation and GA-XANES has been used to investigate the structural stability of glass-ceramic composite materials.

3.2. Experimental

3.2.1. Ion beam implantation

Glass-ceramic composite materials containing brannerite in borosilicate glass or Fe-Al borosilicate glass ($CeTi_2O_6$-BG/FABG) and zirconolite in borosilicate glass or Fe-Al borosilicate glass ($CaZrTi_2O_7$-BG/FABG) were synthesized by the ceramic method (see Section 2.2.1). Glass-ceramic composite materials containing a 30 wt% loading of brannerite/zirconolite in borosilicate glass annealed at 750 ^oC or 1100 ^oC were then implanted with high energy (2 MeV) Au^- ions using the 1.7 MV Tandetron accelerator located at Interface Science Western (ISW), University of Western Ontario.[98] The glass-ceramic composite samples were embedded in a polymer puck prior to implantation and were polished using diamond paste to produce a smooth surface. The polished

side of each glass-ceramic composite bead was implanted to a dose of 5×10^{14} ions/cm^2. The ion beam was aligned normal to the glass-ceramic bead surface during implantation.[98]

3.2.1.1. Calculation of the ion implantation depth profile

The Stopping and Range of Ions in Matter (SRIM-2013) software package was used to calculate the ion implantation depth and defect (number of vacancies) per ion profiles for the implanted materials.[161] The calculation of the ion implantation depth profile was performed using 5000 Au^- ions with the ion beam energy being 2 MeV. The target displacement energies (the minimum energy required to knock a target atom far enough away from its lattice site) for the ion implantation depth profiles were assumed to be 25 eV for Ti/Ce/Zr/Ca and 28 eV for O.[161,162] The densities (ρ) of $CeTi_2O_6$ and $CaZrTi_2O_7$ used in these calculations were 5.11 gr/cm^3 and 4.44 g/cm^3, respectively.[163] The ion implantation depth profiles calculated for ceramic in the glass matrix is similar to the pure ceramics (i.e., $CeTi_2O_6$ and $CaZrTi_2O_7$) based on the assumption that brannerite and zirconolite crystallites were located at the surfaces of the polished glass-ceramic composite beads that were exposed to the Au^- ion beam.

3.2.2. Electron microprobe analysis

Backscattered electron (BSE) images were collected to examine the morphologies of the ion implanted materials using a JEOL 8600 electron microprobe instrument. The samples were coated with a conductive carbon coating prior to introducing them into the instrument.[17] BSE images were collected from the ion implanted glass-ceramic composite materials containing a 30 wt% loading of brannerite in borosilicate glass annealed at 750 ^oC or 1100 ^oC using a magnification of 1000X.

3.2.3. Ti K-edge GA-XANES of the ion-implanted materials

Ti K-edge GA-XANES spectra were collected from the ion implanted (i.e., damaged) glass-ceramic composite beads using the Canadian Light Source/X-ray Science Division Collaborative Access Team (CLS@APS, Sector 20) bending magnetic beamline (20BM) located at the Advanced Photon Source (APS), Argonne National Laboratory.[127] It was necessary to use surface sensitive detection methods to study how the Ti K-edge XANES spectra from these materials change as a result of ion implantation because the implanted ions only penetrated a few hundred nm into the surface of the materials.[17,56,89,96,99] A Si (111) double crystal monochromator with harmonic rejection was used, providing a photon flux of $\sim 10^{11}$ photons/s and a resolution of 0.7 eV at 4966 eV.[17,127] GA-XANES analysis of the ion implanted beads was performed using a vertically focused X-ray beam with a height of 500 μm and a beam width of 50 μm. All spectra were collected in fluorescence mode (FLY) using a single element vortex detector. A motor driven Huber (goniometer) stage was used to change the X-ray beam angle of incidence on the surface of the beads. The stage permits translation in x-, y- and z-axis directions as well as rotation of the sample to change the glancing angle. The glancing angle (α) was set to the desired value with a precision of 0.1^{o} to reach different depths of the ion implanted beads during GA-XANES analysis. The GA-XANES spectra were collected using a step size of 0.15 eV/step through the Ti K-edge and were calibrated using Ti metal (4966 eV).[17,129] A web-based program was used to calculate the glancing angles required to reach specific X-ray attenuation depths for photons having energies of 4966 eV (Table 3.1).[164] All spectra discussed here were normalized, calibrated, and analyzed using the Athena software program.[132]

Table 3.1. Calculated glancing angles required to give specific X-ray attenuation depths for photons having an energy of 4966 eV (Ti K-edge).

	Ti K-edge (4966 eV)	
Sample	**X-ray attenuation depth(nm)**	**Glancing angle (°)**
30 wt% $CeTi_2O_6$ in BG	200	1.0
	400	1.9
	1000	4.7
	6500	31.6
30 wt% $CaZrTi_2O_7$ in BG	200	1.3
	400	2.5
	1000	6.3
	6500	45

3.2.4. Si $L_{2,3}$-edge XANES of the ion-implanted materials

Si $L_{2,3}$-edge XANES spectra were collected from ion implanted composite beads using the Variable Line Spacing-Plane Grating Monochromator (VLS-PGM) beamline at the CLS. The spectra were collected in total fluorescence yield (TFY) mode using a step size of 0.05 eV through the Si $L_{2,3}$-edge. The Si $L_{2,3}$-edge spectra were calibrated using elemental Si (99.4 eV).[17,131]

3.3. Results and discussion

3.3.1. Calculation of the ion implantation depth profiles

The calculated depth profiles predicted that the 2 MeV Au^- ions penetrate through the surface region of the glass-ceramic materials to a maximum depth of ~450 nm (see Figure 3.1 a and b). Profiles of the number of vacancies produced per Au^- ion are shown in Figure 3.1 c and d. These calculations indicate that the maximum number of vacancies (defect per ion) would be

generated at a depth of ~250 nm. Moreover, the number of vacancies decreased dramatically with increasing depth.

3.3.2. Electron microscopy

BSE images from the ion implanted composite materials containing 30 wt% $CeTi_2O_6$ in borosilicate glass annealed at either 750 ^oC or 1100 ^oC are shown in Figure 3.2. The BSE images from the as-synthesized materials containing 30 wt% $CeTi_2O_6$ in borosilicate glass are also shown in this Figure. The BSE images from the implanted (damaged) and as-synthesized (undamaged) glass-ceramic composite materials show that the brannerite crystallites (bright area) can be differentiated from the glass matrix (dark area). Pores were observed in the glass-ceramic composite materials because of air bubble formation during annealing.

The BSE images from the implanted (damaged) composite materials containing 30 wt% $CeTi_2O_6$ in borosilicate glass annealed at 1100 ^oC (Figures 3.2d) contained smaller crystallites when compared to the images from the implanted (damaged) composite materials annealed at 750 ^oC (Figures 3.2c). These observations are in good agreement with the backscattered images from the as-synthesized (undamaged) composite materials (see Section 2.3.2). The comparison of the BSE images from the composite materials containing brannerite before (Figures 3.2a and 3.2b) and after ion implantation (Figures 3.2c and 3.2d) show no (apparent) changes in morphology or grain size of the brannerite-type (brighter area) crystallites in the glass-ceramic composite materials upon ion implantation. This observation indicates that ion implantation does not significantly affect the morphology of the crystallites in the glass matrix.

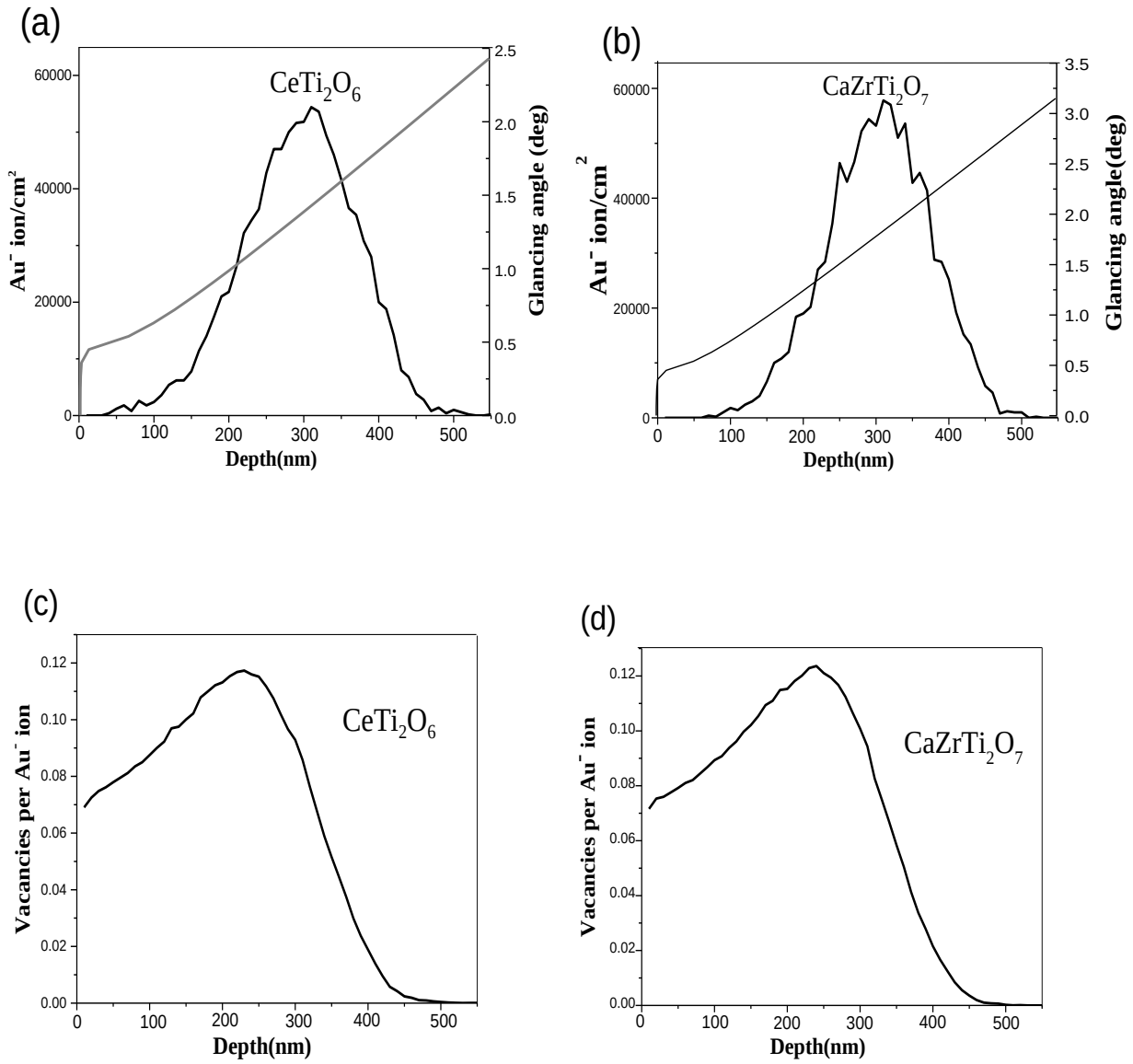

Figure 3.1. Plots of the ion beam implantation depth profiles from (a) $CeTi_2O_6$ and (b) $CaZrTi_2O_7$ calculated using SRIM-2013 are shown.[161] The calculations were performed using 5000 Au^- ions with the ion beam energy being 2 MeV. The plots of glancing angle *versus* X-ray attenuation depth for brannerite and zirconolite are also included in the figures and were calculated for photons having an energy of 4966 eV (Ti K-edge). The calculations predicted that the ion beam implants to a depth of 100-450 nm for all samples. The plots of the number of vacancies produced per Au^- ion (defect per ion profile) in (c) $CeTi_2O_6$ and (d) $CaZrTi_2O_7$ by a 2 MeV beam of 5000 Au^- ions are presented.

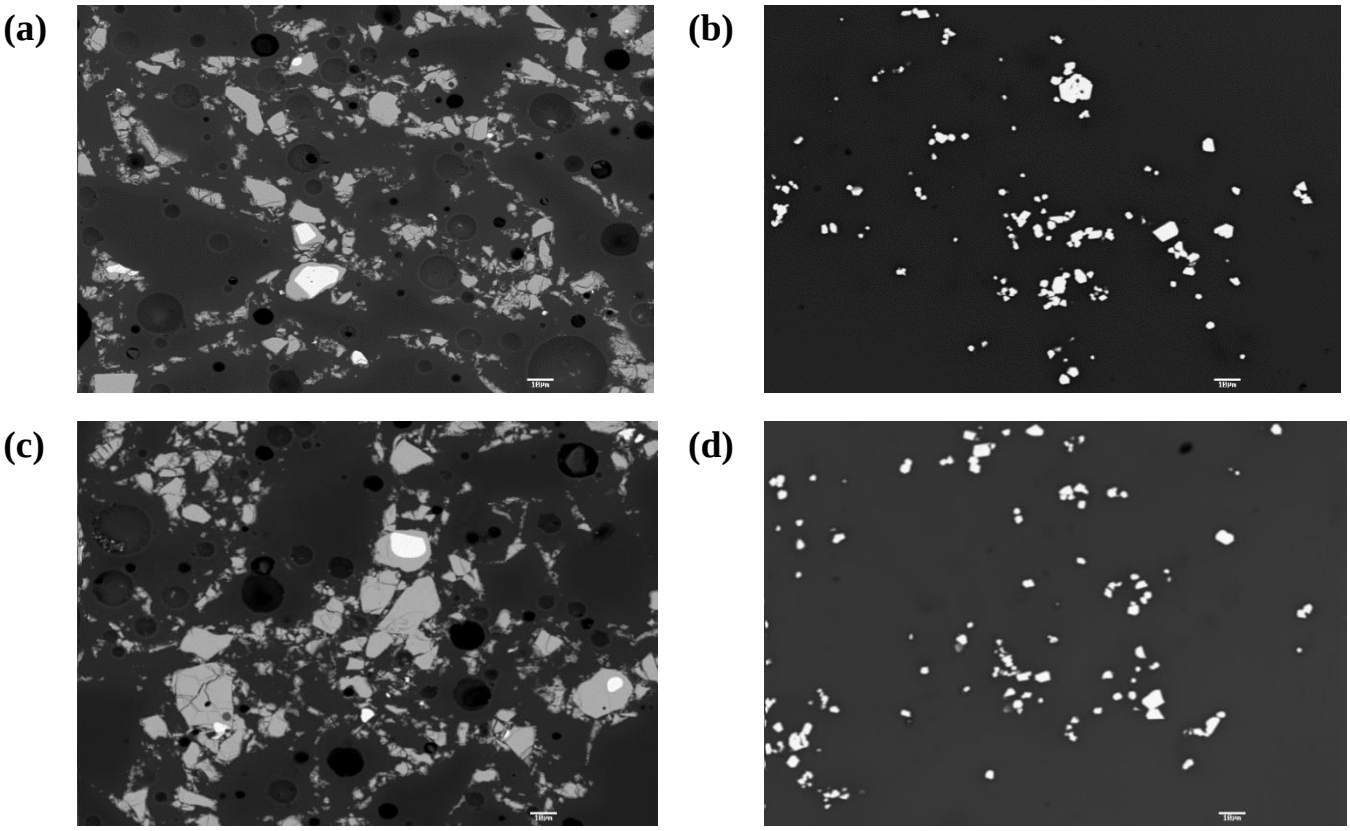

Figure 3.2. Backscattered images from (a) as-synthesized and (c) ion-implanted composite materials containing 30 wt% $CeTi_2O_6$ in borosilicate glass annealed at 750 ^oC, (b) as-synthesized and (d) ion-implanted composite materials containing 30 wt% $CeTi_2O_6$ in borosilicate glass annealed at 1100 ^oC are shown. The scale bar in each image is 10 μm.

3.3.3. Ti K-edge GA-XANES spectra from the ion-implanted materials

Ti K-edge GA-XANES spectra were collected from the ion implanted composite materials to study how the local environment of Ti in these materials change as a result of ion implantation. Ti K-edge spectra result from 1s→3d (quadrapolar; pre-edge (A)) and 1s→4p (dipolar; main-edge (B and C)) transitions.[54,55] Three features are observed in the pre-edge region (labeled as A_1, A_2, and A_3), which result from both local and non-local excitations. A detailed description for these features was presented in Section 2.3.3.1. As was discussed previously, the intensity of the pre-edge feature (A) increases while the energy (B) and intensity (C) of the main-edge features decrease with decreasing Ti coordination number (CN).[56-60] It was shown in Chapter 2 that the

local structure of Ti in the glass-ceramic composite materials was affected strongly by annealing temperature. The composite materials containing brannerite or zirconolite crystallites annealed at 1100 ^{o}C showed a lower Ti CN compared to the composite materials annealed at 750 ^{o}C because more crystallites dissolved in the glass after annealing at 1100 ^{o}C. All GA-XANES spectra for the implanted materials were collected in fluorescence mode because of the thickness of the implanted pellets (~1-2 mm), and because only the near-surface region of the materials was affected by ion implantation.

3.3.3.1. Ti K-edge GA-XANES spectra from ion-implanted brannerite-containing composites

The Ti K-edge GA-XANES spectra from the ion-implanted brannerite-containing composite materials were collected using glancing angles of 1.0^{o}, 1.9^{o}, 4.7^{o}, and 31.6^{o}, which provide X-ray attenuation depths of 200 nm, 400 nm, 1000 nm and 6500 nm, respectively.[164] The surface sensitivity of GA-XANES spectra increases with decreasing glancing angle.[89,121-123] Normalized Ti K-edge GA-XANES spectra from the ion implanted composite beads (30 wt% $CeTi_2O_6$ in BG) annealed at either 750 or 1100 ^{o}C using Au^- ions to a dose of 5×10^{14} ions/cm^2 are shown in Figures 3.3a and 3.3b. The spectra from the as-synthesized materials (30 wt% $CeTi_2O_6$-BG) annealed at either 750 or 1100 ^{o}C are also presented in these figures. It was observed that the intensity of the pre-edge feature (A) increased while the energy (B) and intensity (C) of the main-edge features decreased with decreasing glancing angel used to collect the Ti K-edge GA-XANES spectra from the implanted (damaged) composite materials when compared to the spectra from the as-synthesized materials (see Figures 3.3). An observed increase in the intensity of feature A and decrease in the energy of feature B when comparing the implanted (damaged) composite materials to the as-synthesized (undamaged) composite materials can be attributed to a lowering of the average Ti CN (see Section 2.3.3.1).[17,83,118,138-141]

A comparison of the Ti K-edge GA-XANES spectra collected at different glancing angles from the implanted composite materials show that more damage (i.e., lower Ti CN) occurs near the surface compared to deeper into the material.[17] The observed reduction of the Ti CN suggests that the atoms in the near-surface region of the glass-ceramic materials become disordered upon ion implantation.[17] Comparing the spectra from the implanted composites (30 wt% $CeTi_2O_6$-BG) annealed at either 1100 ^oC (Figure 3.3a) or 750 ^oC (Figure 3.3b) shows that structural damage occurs as a result of ion implantation in these glass-ceramic composite materials regardless of annealing temperature.

3.3.3.2. Ti K-edge GA-XANES spectra from ion-implanted zirconolite-containing composites

The Ti K-edge GA-XANES spectra from the ion-implanted zirconolite-containing composite materials (30 wt% $CaZrTi_2O_7$-BG) annealed at either 750 or 1100 ^oC using Au^- ions to a dose of 5×10^{14} ions/cm^2 are shown in Figures 3.4a and 3.4b. Glancing angles of 1.3^o, 2.5^o, 6.3^o, and 45^o were used to collect the Ti K-edge GA-XANES spectra from these materials which provides X-ray attenuation depths of 200 nm, 400 nm, 1000 nm and 6500 nm, respectively.[164] An increase in the intensity of the pre-edge feature (A) and a decrease in energy and intensity of the main-edge features (B,C) were observed from the implanted materials when compared to the spectra from the as-synthesized materials. Comparing the intensity of the pre-edge (A) and energy of the main edge (B) from the ion implanted (damaged) to the as-synthesized (undamaged) materials suggests that the local CN of Ti decreased after ion implantation.[17,138-141] As the glancing angels used to collect spectra from the ion implanted materials decreased, more damage of the structure of the ceramics occurred (i.e., lower Ti CN). These observations show that the local structure of Ti in the zirconolite-containing glass-ceramic composite materials is affected by ion implantation. A comparison of the Ti K-edge XANES spectra from both implanted composite

materials (30 wt% $CeTi_2O_6$-BG and 30 wt% $CaZrTi_2O_7$-BG) show that the structures of the ceramics are damaged as a result of ion implantation of the composite materials containing different ceramic crystallites.

3.3.4. Si $L_{2,3}$-edge XANES spectra from the ion-implanted materials

Si $L_{2,3}$-edge XANES spectra were collected from the ion implanted glass-ceramic composite materials to study how the local structure of Si in the glass matrix is affected by ion implantation. The Si $L_{2,3}$-edge XANES spectra contain two features that result from 2p→3s (Feature D) and 2p→3d (Feature E) transitions, respectively. The low-energy feature (D) is split into two peaks (D_1 and D_2) due to spin-orbit splitting.[149,150] The Si $L_{2,3}$-edge XANES spectra from the ion implanted composite beads (30 wt% $CeTi_2O_6$ /$CaZrTi_2O_7$ in BG) annealed at 750 or 1100 ^oC are shown in Figure 3.5. The spectra from the as-synthesized composite materials are also presented in these figures. It was shown in Chapter 2 that the silicate network was affected depending upon the loading of $CeTi_2O_6$ or $CaZrTi_2O_7$, annealing temperature, and the type of glass used to form these composite materials (see Section 2.3.3.4). Examination of the Si $L_{2,3}$-edge XANES spectra from the Au^- ion implanted composite beads (30 wt% $CeTi_2O_6$ /$CaZrTi_2O_7$ in BG) annealed at 750 or 1100 ^oC shows negligible changes in the spectral features (D and E) compared to the as-synthesized composite materials. This observation suggests that ion implantation does not significantly affect the local structure of the glass in these composite materials.

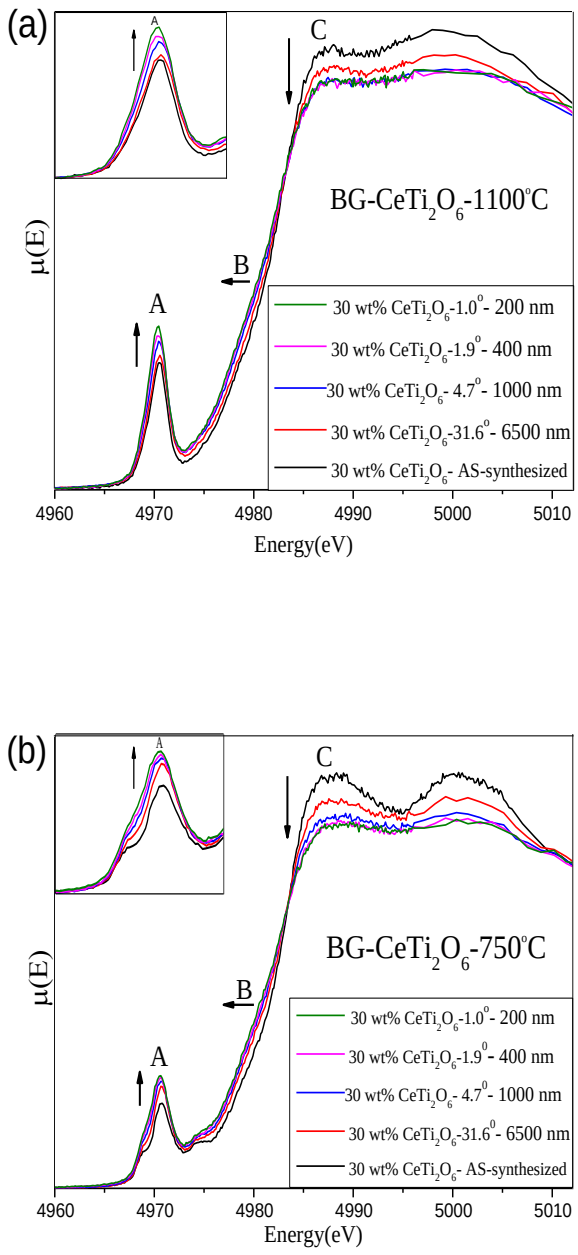

Figure 3.3. Ti K-edge GA-XANES spectra from (a) BG-$CeTi_2O_6$-1100 ºC and (b) BG-$CeTi_2O_6$-750 ºC containing 30 wt% loading of $CeTi_2O_6$ implanted using Au^- ions to a dose of 5×10^{14} ions/cm^2 are shown. The spectra from the as-synthesized composite materials are also presented. The angles listed, 1.04º, 1.90º, 4.67º, and 31.65º, are the glancing angles used to attain X-ray attenuation depths of 200 nm, 400 nm, 1000 nm and 6500 nm, respectively. The changes observed in the spectra with decreasing glancing angle are indicated by arrows.

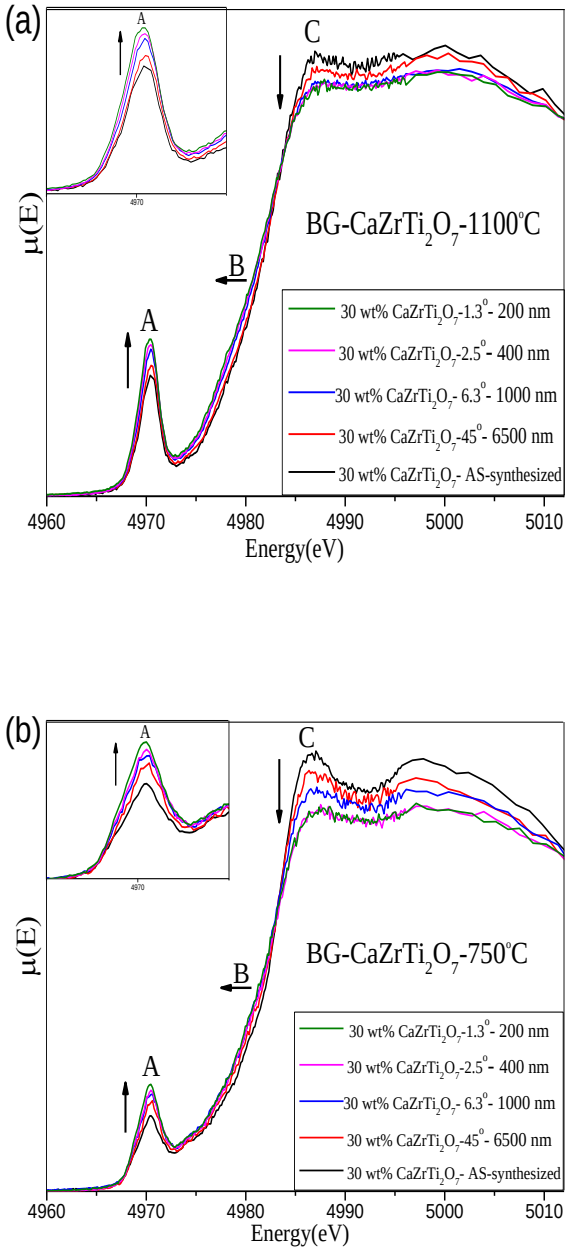

Figure 3.4. Ti K-edge GA-XANES spectra from (a) BG-$CaZrTi_2O_7$-1100 ºC and (b) BG-$CaZrTi_2O_7$-750 ºC containing 30 wt% loading of $CaZrTi_2O_7$ implanted using Au^- ions to a dose of 5×10^{14} ions/cm^2 are shown. The spectra from the as-synthesized composite materials are also presented. The angles listed, 1.34º, 2.53º, 6.30º, and 45.00º, are the glancing angles used to attain X-ray attenuation depths of 200 nm, 400 nm, 1000 nm and 6500 nm, respectively. The changes observed in the spectra with decreasing glancing angle are indicated by arrows.

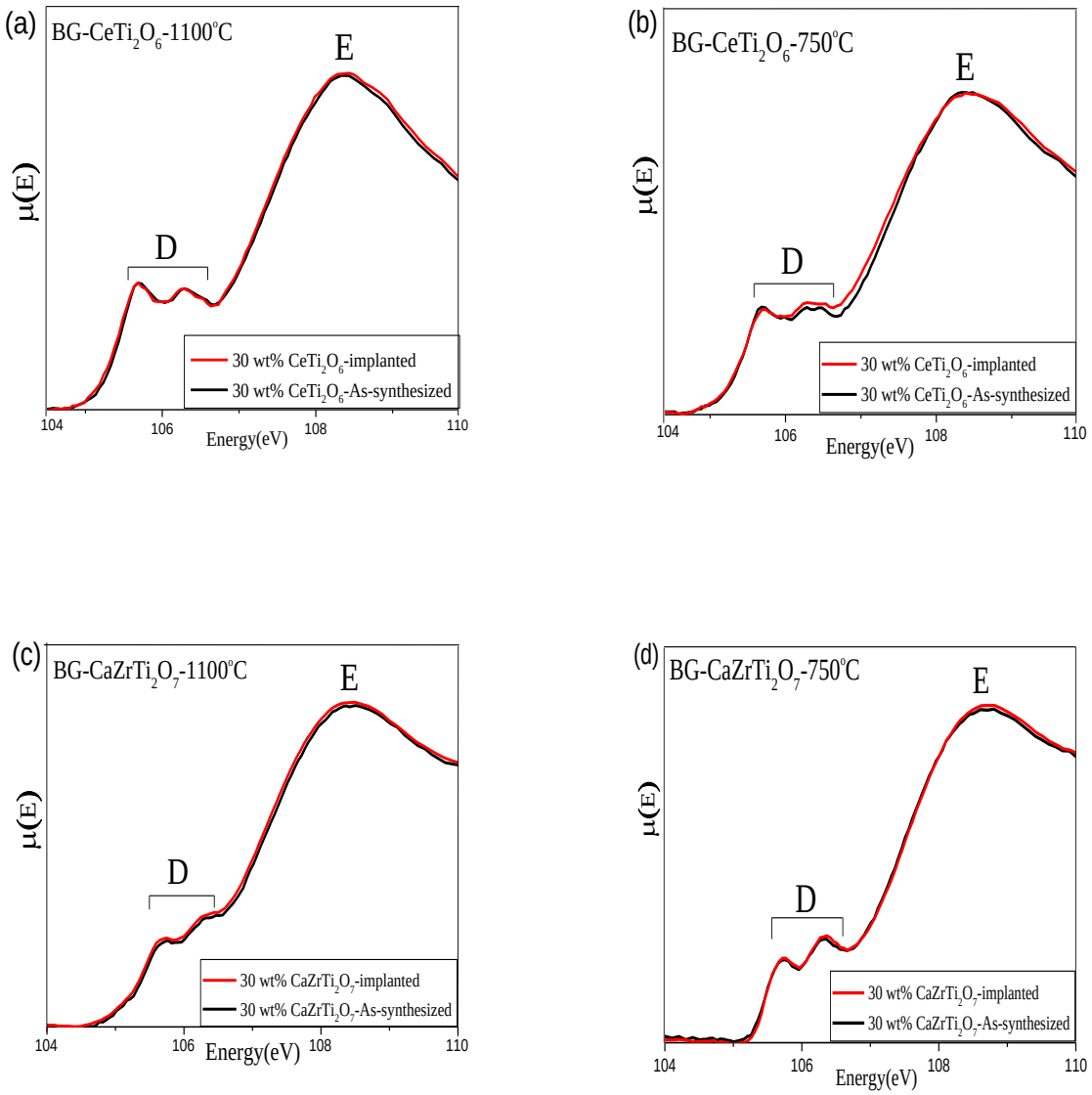

Figure 3.5. Si $L_{2,3}$-edge XANES spectra from ion implanted composites (a) BG-30 wt% $CeTi_2O_6$-1100 ºC, (b) BG-30 wt% $CeTi_2O_6$-750 ºC, (c) BG-30 wt% $CaZrTi_2O_7$-1100 ºC and (d) BG-30 wt% $CaZrTi_2O_7$-750 ºC are shown. These spectra are compared to the spectra from the as-synthesized composite materials.

3.4. Conclusions

Glass-ceramic composite materials were implanted with high-energy (2 MeV) heavy ions (Au^- ions) to mimic radioactive decay of incorporated nuclear waste elements. The objective of this study was to understand how the structure of a glass-ceramic composite wasteform responds to the radioactive decay of incorporated nuclear waste elements. A combination of ion implantation and GA-XANES has been used to investigate the structural stability of the glass-ceramic composite materials. Surface sensitive GA-XANES have been successfully demonstrated to probe the damaged surface layer of glass-ceramic composite materials after being implanted by heavy ions (Au^- ions). Examination of Ti K-edge GA-XANES spectra from ion implanted composite materials containing brannerite and zirconolite in borosilicate glass annealed at 750 or 1100 ^oC have shown that ion implantation damages the structure of the ceramics in the composite materials. A comparison of the Ti K-edge spectra from the composite materials containing brannerite or zirconolite crystallites show that similar changes in the coordination environment of Ti occur as a result of ion implantation. The study of Si $L_{2,3}$-edge XANES spectra from the ion implanted composite materials containing brannerite and zirconolite in borosilicate glass annealed at 750 or 1100 ^oC have shown that ion implantation does not appear to alter the glass structure in these composite materials. Comparing the backscattered electron images from the composite materials containing brannerite crystallites before and after ion implantation have shown that morphology or grain size of the crystallites in the glass-ceramic composite materials does not change upon ion implantation. It is expected that the damage experienced by a ceramic in a glass matrix *vs.* the pure ceramic will be similar because ion implantation affects the local structure (e.g., coordination number) of ceramics and glass-ceramic materials in a similar way.[17] This study has

provided a better understanding of how changes in the glass and ceramic composition can affect the resistance of glass-ceramic composite materials to radiation induced structural damage.

Chapter 4

Conclusions and directions for future research

4.1. Effect of combining ceramics with glass materials

The work presented in Chapter 2 has examined different factors affecting the structure of glass-ceramic composite materials. Structural characterization techniques have been used to successfully probe the long-range and local structure of glass-ceramic materials. Borosilicate and Fe-Al-borosilicate glass-ceramic composites containing brannerite ($CeTi_2O_6$) or zirconolite ($CaZrTi_2O_7$) crystallites were synthesized at different annealing temperatures to study the effect of composition and annealing temperature on the local and long-range structure of these materials. Powder X-ray diffraction (XRD) and backscattered electron (BSE) images were used to study the dispersion of ceramic crystallites in the glass matrix. XRD patterns from borosilicate glass composite materials containing brannerite or zirconolite annealed at either 750 or 1100 ^oC indicated that a significant amount of the ceramic crystallites (i.e., brannerite or zirconolite) dissolved in the glass matrix after annealing at 1100 ^oC. Comparing the XRD patterns from borosilicate and Fe-Al borosilicate glass composite materials annealed at either 750 or 1100 ^oC showed that the type of glass used (i.e., borosilicate or Fe-Al borosilicate) does not influence how the annealing temperature affected the average structure of these composite materials. Backscattered electron images collected from the composite materials confirmed that more brannerite/zirconolite crystallites dissolved in the glass matrix after annealing at higher temperatures (i.e., 1100 vs 750 ^oC). The BSE images were in good agreement with the analysis of the XRD patterns.

XANES has provided great insight into changes in the local environment of glass-ceramic composite materials that occur as a result of changing the synthesis conditions. Examination of Ti

K-edge XANES spectra from the composite materials indicated that the average Ti CN was lower in the composites annealed at 1100 ^{o}C compared to the composites annealed at 750 ^{o}C, further confirming that more ceramic dissolved in the glass matrix after annealing at 1100 ^{o}C. Comparing the Ti K-edge XANES spectra from borosilicate and Fe-Al borosilicate glass composite materials showed that the coordination environment of Ti was not affected by changing the type of glass used to form these composite materials. Examination of Ce L_3-edge XANES spectra from the BG-$CeTi_2O_6$ composite materials indicated that the major oxidation state of Ce was 4+ for all composite materials annealed at 750 ^{o}C while the concentration of Ce^{3+} increased with decreasing loading of brannerite in the BG-$CeTi_2O_6$ composite materials annealed at 1100 ^{o}C. Zr K-edge spectra were collected from the composite materials containing $CaZrTi_2O_7$ in order to understand how the Zr CN in the BG-$CaZrTi_2O_7$ composites was affected by the synthesis conditions used to form these materials. Comparing the Zr K-edge XANES spectra from the glass-ceramic composite materials showed that the average Zr CN was lower in the composites annealed at 1100 ^{o}C compared to the composite materials annealed at 750 ^{o}C. As the annealing temperature increased, the CN of Zr decreased in the composites because zirconolite crystallites dissolved in the glass matrix. Si $L_{2,3}$-edge XANES spectra showed that the ordering of the silicate network can be affected depending upon the loading of $CeTi_2O_6$ or $CaZrTi_2O_7$, annealing temperature, and the type of glass used to form these composite materials. Comparing the Si $L_{2,3}$-edge XANES spectra from borosilicate and Fe-Al borosilicate glass composite materials annealed at either 750 or 1100 ^{o}C indicated that the silicate environment in the borosilicate glass matrix was affected to a greater degree than in the Fe-Al borosilicate glass matrix because of the partial crystallization of the borosilicate glass and next nearest-neighbour effects. Examination of Fe K-edge XANES spectra from the composite materials indicated that the Fe oxidation state changed with varying annealing

temperature. The oxidation state of Fe in the composite materials annealed at 1100 ^{o}C was reduced to 2+ while the oxidation state of Fe in the composite materials annealed at 750 ^{o}C was 3+. Investigating all XANES spectra showed that the $CeTi_2O_6$ or $CaZrTi_2O_7$ crystallites can dissolve in the glass matrix depending on the ceramic loading, the glass composition, and the annealing temperature used to form these composite materials. Similar changes in the long-range and local structure of the glass-ceramic composite materials containing brannerite or zirconolite were observed when the synthesis conditions to form these materials were changed.

Studying behaviour of glass-ceramic composite materials with changing synthesis conditions has provided a good framework of how variation in the synthesis conditions (i.e., changing the ceramic loading, the glass composition, and the annealing temperature) can affect the local structure of these composite materials. This study is important for designing and developing composite materials as nuclear wasteforms with optimal performance for the immobilization of nuclear waste. For example, a low annealing temperature (i.e., 750 ^{o}C) was more favourable to the formation of a composite material with a negligible amount of the ceramic having dissolved in the glass matrix. At a higher annealing temperature (i.e., 1100 ^{o}C), higher loading of ceramic was required for the formation of a desirable glass-ceramic composite material. The chemistry of ceramic crystallites within the glass matrix was also affected by glass composition because of changes in the ordering of the glass and next nearest-neighbour effects. For glass-ceramic composite materials to be a potential nuclear wasteform, they should have a homogeneous distribution of crystalline materials in the bulk of a glass matrix which was observed by BSE images from the composite materials studied here after annealing them at 750 ^{o}C or 1100 ^{o}C.

4.2. Effect of changes in composition on structural stability

The effect of radiation induced structural damage depending on the composition of glass-ceramic composite materials was investigated in Chapter 3. The glass-ceramic composite materials were implanted with high-energy (2 MeV) heavy ions (Au^- ions) to mimic radiation induced damage. A combination of ion implantation and GA-XANES was used to investigate the structural stability of glass-ceramic composite materials. Surface sensitive GA-XANES have been successfully demonstrated to probe the damaged surface layer of a material after being implanted by heavy ions. This will help to investigate how the structure of a material responds to the radioactive decay of incorporated nuclear waste elements. The comparison of the BSE images from the composite materials containing brannerite before and after ion implantation showed that similar morphologies of the $CeTi_2O_6$ and $CaZrTi_2O_7$ crystallites appear in the glass matrix. Examination of Ti K-edge GA-XANES spectra from ion implanted composite materials containing brannerite or zirconolite in borosilicate glass showed that ion implantation damaged the structure of the ceramics in the composite materials regardless of annealing temperature. However, the study of Si $L_{2,3}$-edge XANES spectra from the ion implanted composite materials showed that ion implantation does not appear to affect the glass structure in these composite materials. This study has shown the susceptibility of these glass-ceramic composite materials to radiation induced structural damage and has provided a better understanding of how to design materials for immobilization of nuclear waste.

4.3 Directions for Future Research

Studying glass-ceramic composites containing $CeTi_2O_6$ or $CaZrTi_2O_7$ crystallites was a good starting point for further exploration of the electronic structures and thermal stability of these materials. Investigating various glass-ceramic composite systems could be considered for future

research to understand how the structure, long-range order, and morphology of these materials vary with changing synthesis conditions. There are many glass-ceramic composite systems that need to be studied. The combination of different types of ceramic crystallites (i.e., hollandite or perovskite) and glass composition (i.e., silicate or phosphate glasses) and different annealing temperatures should be studied to understand the effect of synthesis conditions on the structural and electronic properties of the composite materials. Different synthesis methods (i.e., sol-gel method, concurrent sinter-crystallization of glass-particles, etc.) could be used to synthesize glass-ceramic composite materials for different application. For example, the sol-gel method has been used to fabricate glass-ceramic composite materials for dental applications.[165]

A wide range of glass-ceramic composite materials could be implanted with high energy heavy ions to mimic radiation induced structural damage. It is expected that the degree of resistance to structural damage varies with changing ceramic and glass composition.[17] It was shown previously that adding ZnO to borosilicate glass can enhance the stability of a glass structure, which would affect the radiation resistance of a Zn-borosilicate glass composite material.[166-168] Zn as a network intermediate can stabilize the amorphous structure of the glass.[134-136,166-168] Zn-borosilicate glass composite materials containing brannerite, zirconolite, hollandite or pyrochlore could be chosen to study the effect of glass composition on the structural and electronic properties of the composite materials.

The glass-ceramic composite materials could be investigated using extended X-ray absorption fine structure (EXAFS) and X-ray photoelectron spectroscopy (XPS) as well. EXAFS can be used to provide information on the number and chemical identities of neighbouring atoms around the absorbed atom. X-ray photoelectron spectroscopy (XPS) can also be used to probe the

surface area of materials. This yields information about the elemental composition, chemical state and electronic state of the elements that exist within a material.

This thesis has given more insights into the chemistry of ceramic materials within a glass matrix and will provide a better understanding of how to develop and design materials for sequestration applications as well as for other applications.

5. References

1. Shaw, A.; Sriramula, S.; Gosling, P.D.; Chryssanthopoulo, M. K. *Composites Part B.* **2010**, 41, 446–453.

2. Boccaccini, A. R.; Ferraris, M.; Reece, M. J.; Salvo, M. *Adv. Appl. Ceram.* **2015**, 114, 6753-6761.

3. El-Meliegy, E.; van. Noort, R. *Glasses and Glass Ceramics for Medical Applications;* Springer Science: New Yourk, USA, **2012**.

4. Digeos, A. A.; Valdez, J. A.; Sickafus, K. E.; Atiq, S.; Grimes, R. W.; Boccaccini, A. R. *J. Mater. Sci.* **2003**, 38, 1597-1604.

5. Lee, W. E.; Ojovan, M. I.; Stennett, M. C.; Hyatt, N. C. *Adv. Appl. Ceram.* **2006**, 105, 1-12.

6. Loiseau, P.; Caurant, D. *J. Nucl. Mater.* **2010**, 402, 38-54.

7. Boccaccini, A. R.; Bernardo, E.; Blain, L.; Boccaccini, D. N. *J. Nucl. Mater.* **2004**, 327, 148-158.

8. Caurant, D.; Loiseau, P.; Bardez, I.; Gervais, C. *J. Mater. Sci.* **2007**, 42, 8558-8570.

9. He, Y.; Bao, W.; Song, C. *J. Nucl. Mater*. **2002**, 305.

10. Zhang, Y.; Zhang, Z.; Thorogood, G.; Vance, E. R. *J. Nucl. Mater.* **2013**, 432, 545-547.

11. Hölland, W.; Rheinberger, V.; Schweiger, M. *Phil. Trans. R. Soc. Lond.* **2003**, 361, 575–589.

12. McMillan, P.W. *Non-Metallic Solids*. Academic Press Inc, **1979**.

13. Hölland, W.; Beall, G. *American Ceramic Society*, Wiley, OH, **2002**.

14. Strnad, Z. *Glass-Ceramic Materials*. Elsevier, Amsterdam, **1986**.

15. Stooky, S .D. *J. Ind. Eng. Chem*. **1959**, 1, 805-808.

16. Shackelford, J. F.; Doremus, R. H. *Ceramic and Glass Materials*. Springer Scienc, **2008**.

17. Aluri, E. R.; Grosvenor, A. P. *RSC Adv.* **2015**, 5, 10477-10486.

18. Peitl, O.; Zanotto, E. D.; Hench, L. L. *J. Non-Cryst. Solids*. **2001**, 292, 115–26.

19. Marshall, D.; Cox, Brian. *Textile Composite Materials*, Wiley, **2010**.

20. Ko, F. K.; Du, G. W. *Handbook of Composites*. **1998**, 397-424.

21. Shishoo, R. L. *Indian J Fibre Text Res.* **1997**, 22, 213-221.

22. Shamsudin, Z.; Hodzic, A.; Soutis, C.; Hand, R. J.; Bond, I. P.; Howard, P. J.; Szkoda, I. *Adv. Polym. Compos. Sci*. **2015**, 1, 120-127.

23. Scardino, F. *Textile Structural Composites*. Elsevier, **1989**, 1-24.

24. Grande, D. H.; Mandell, J. F.; Hong, K. C. C. *J. Mater.Sci*. **1988**, 23, 311-328

25. Sambell, R. A. J.; Briggs, A.; Phillips, D. C.; Bowen, D. H . *J. Mater. Sci.*, **1972**, **7**, 676–681.

26. Ewing, R. C. *Proc. Natl. Acad. Sci*. **1999**, 96, 3432-3439.

27. Ojovan, M. I.; Juoi, J. M.; Lee, W. E. *J Pak Mater Soc*. **2008**, 2, 72-76.

28. Amoroso, J.; Marra, J. C.; Tang, M.; Lin, Y.; Chen, F.; Su, D.; Brinkman, K. S. *J. Nucl. Mater.* **2014**, 454, 12-21.

29. Ewing, R. C.; Weber, W. J.; Clinard, F. W. *Prog. Nucl. Energy*. **1995**, 29, 63-121.

30. Lumpkin, G. R.; Whittle, K. R.; Rios, S.; Smith, K. L.; Zaluzec, N. J. *Journal of Physics Condensed Matter*. **2004**, 16, 8557-8570.

31. Boccaccini, A. R.; Atiq, S.; Grimes, R. W. *Adv. Eng. Mater.* **2003**, 5, 501-508.

32. Forsberg, C. W. *Progress in Nuclear Energy*. **2008**, 1–9.

33. Dunlap, R. E.; Kraft, M. E.; Rosa, E. A. *Citizens' views of repository siting*. Duke University Press, **1993**.

34. Weber, W. J.; Navrotsky, A.; Stefanovsky, Sergey.; Vance, E. R.; Vernaz, E. *Mrs Bulletin.* **2009**, 34 , 46-53.

35. Guérin, Y.; Was, G. S.; Zinkle, S. *Mrs bulletin*. **2009**, 34, 10-19.

36. Lutze, W.; Ewing, R. C. *Radioactive Waste Forms for the Future*. Netherlands: Amsterdam, **1988**.

37. Cohen, B. L. *Rev. Mod. Phys*. **1977**, 49, 1.

38. Mueller, I.; Weber, W. J. *MRS Bull.* **2001**, 26, 698.

39. Baisden, P. A.; Choppin, G. R. Nuclear Waste Management and the Nuclear Fuel Cycle. **2007**.

40. *Inventory of Radioactive Waste in Canada*. Annual Report-01613-041-10003; Ottawa, Canada, **2012.**

41. *Disposal of High Level radioactive Waste in Geologic Repositories*, Code of Federal Regulations-10CFR60; Department of the Energy, Canada, **2003**, 10, 0-199.

42. Mincher, B. J. *Radiation chemistry in the reprocessing and recycling of spent nuclear fuels*, Woodhead Publishing Series in Energy, United States, **2015**.

43. US Nuclear Regulatory Commission. http://www.nrc.gov/waste/spent-fuel-storage/pools.html

44. McKay, H. A.C. *Nuclear fuel cycle*. IAEA bulletin, **1987**, 23, 46-49.

45. *Safety and Security of Commercial Spent Nuclear Fuel Storage:* Public Report 2006, The National Academies Press: Washington, DC, **2006**.

46. Falck, W. E.; Nilsson, K. F. *Geological Disposal of Radioactive Waste*. Institute for Energy, Netherlands, **2009**.

47. Ramana, M. V. *Energy Policy.* **2013**, 61, 196–206.

48. Ahn, J.; Apted, M. J. *Geological Repository Systems for Safe Disposal of Spent Nuclear Fuels and radioactive waste*. Woodhead publishing limited, UK, **2010**, 261-271.

49. Ewing, R. C.; Von Hippel, F. N. *Science.* **2009**, *325*, 151-152.

50. *Developing Multinational Radioactive Waste Repositories*: Infrastructural Framework and Scenarios of Cooperation, IAEA-TECDOC-1413, IAEA, Vienna, **2004**.

51. Burakov, B. E. *Proc. Safe waste*, **1993**, 2, 19 –28.

52. Laverov, N. P.; Yudintsev, S. V.; Livshits, T. S.; Stefanovsky, S. V.; Lukinykh, A. N.; Ewing, R. C. *J. Geochemistry International.* **2010**, 48, 1-14.

53. Lian, J.; Wang, L. M.; Lumpkin, G. R.; Ewing. R. C. *Nuclear Instruments and Methods in Physics Research B.* **2002**, 191, 565-570.

54. Raj, K.; Kaushik, C. P. IOP Conf. Ser.: *Mater. Sci. Eng*. **2009**, 2, 1-6.

55. Ojovan, M. I.; Lee, W. E. *Metallurgical and Materials Transactions.* **2011**, 42, 837-851.

56. Weber, W. J.; Ewing, R. C.; Catlow, C. R. A.; Rubia, T. D.; Hobbs, L. W.; Kinoshita, C.; Matzke, Hj.; Motta, A. T.; Nastasi, M.; Salje, E. K. H.; et al. *J. Mater. Res.* **1998**, 13, 1434-1484.

57. Ewing, R. C.; Weber, W. J.; Lian, J. *J. Appl. Phys.* **2004**, 95, 5949-5971.

58. Sickafus, K. E.; Grimes, R. W.; Valdez, J. A.; Cleave, A.; Tang, M.; Ishimaru, M.; Corish, S.; Stanek, C. R.; Uberuaga, B. P. *Nature Mater.* **2007**, 6, 217-223.

59. Watkins, G. D.; Troxell, J. R.; Chatetjee, A. P. *Defects and Radiation Effects in Semiconductors*. Conf. Ser, **1978**, 16.

60. Ewing, R. C.; Meldrum, A.; Wang, L.; Wang, S. *Rev. Mineral. Geochem*. **2000**, 39, 319-361.

61. Thome, L.; Garrido, F. *Vacuum*, **2001**, *63*, 619–626.

62. Hobbs, L. W.; Clinard, F. W.;. Zinkle, S. J.; Ewing, R. C. *Journal of Nuclear Materials*. **1994**, 216, 291-321.

63. Donald, I. W. *Waste Immobilization in Glass and Ceramic Based Hosts*; John Wiley & Sons Ltd: UK, **2010**, 101-328.

64. Grambow, B. *Elements*. **2006**, 2, 357–364.

65. Donald, I. W.; Metcalfe, B. L.; Taylor, R. N. J. *J. Mater. Sci*. **1997**, 32, 5851–5887

66. Paul, A. *Chemistry of Glasses.* Chapman & Hall: New York, **1990**.

67. Ojovan, M. I.; Lee, W. E. *An Introduction to Nuclear Waste Immobilization*; Elsevier: Amsterdam, **2005**.

68. Marples, J. A. C. *Glass Technol*. **1988**, 29, 230.

69. McGann, O. J.; Bingham, P. A.; Hand, R. J.; Gandy, A. S.; Kavcic, M.; Zitnik, M.; Bucar, K.; Edge, R.; Hyatt, N. C. *J. Nucl. Mater.* **2012**, 429, 353-367.

70. Malchukova, E.; Boizot, B.; Petite, G.; Ghaleb, D. *Eur. Phys. J. Appl. Phys.* **2009**, 45, 10701-10710.

71. McGann, O. J.; Gandy, A. S.; Bingham, P. A.; Hand, R. J.; Hyatt, N. C. *MRS Proc.* **2013**, 1518, 41-46.

72. Lumpkin, G. R. *Elements.* **2006**, *2*, 365–372.

73. Smith, K. L.; Zaluzec, N. J.; Lumpkin. G. R. *Journal of Nuclear Materials.* **1997**, 250, 36-52.

74. Ewing, R. C. *Canad. Mineral.* **2001**, *39*, 697-715.

75. Ewing, R. C.; Jercinovic, M. J. *MRS Proc.* **1986**, *84*, 67.

76. Clinard, F. W.; Rohr, D. L.; Roof, R. B. *Nuclear Instruments and Methods in Physics Research B 1*, **1984**, 581-586.

77. Wang, L.; Liang, T. *J. Adv. Ceram.* **2012**, 3, 194-203.

78. Weber, W. J.; Roberts, F. P. A. *Nucl. Tech.*, **1983**, 60, 178-198.

79. Ringwood, A. E.; Oversby, V. M.; Kesson, S. E.; Sinclair, W.; Ware, N.; Hibberson, W.; Major, A. *Nucl. Chem. Waste Manage.* **1981**, 2, 287-305.

80. Lumpkin, G. R.; Smith, K. L.; Blackford, M. G. *J. Nucl. Mater*. **2001**, 289, 177-187.

81. Helean, K. B.; Navrotsky, A.; Lumpkin, G. R.; Colella, M.; Lian, J.; Ewing, R. C.; Ebbinghaus, B.; Catalano, J. G. *J. Nucl. Mater*. **2003**, 320, 231-244.

82. Lopez, C.; Deschanels, X.; Bart, J. M.; Boubals, J. M.; Den Auwer, C.; Simoni, E. *J. Nucl. Mater*. **2003**, 312, 76-80.

83. Huynh, L. T.; Eger, Sh. B.; Walker, J. D. S.; Hayes, J. R.; Gaultois, M. W.; Grosvenor, A. P. *Solid State Sciences*. **2012**, 14, 761-767.

84. Momma K.; Izumi, F. *J. Appl. Crystallogr.* **2008**, 41, 653-658.

85. Stefanovsky, S. V.; Nikokov, B. S.; Omelianenko, B. I.; Yudintsev, S. V.; Yakushev, A. I. *Phys. Chem. Mat. Treat*. **1997**, 111-117.

86. Yudintsev, S. V.; Omelianenko, B. I.; Stefanovsky, S. V.; Ochkin, A. V.; Chizhevskaya, S. V. *J. Adv. Mat*. **1998**, 91-100.

87. Caurant, D.; Loiseau, P.; Bardez, I. *Journal of Nuclear Materials*. **2010**, 407, 88-99.

88. Zhang, Y.; Stewart, M. W. A.; Li, H.; Carter, M. L.; Vance, E. R.; Moricca, S. *J. Nucl. Mater*. **2009**, 395, 69-74.

89. Reid, D. P.; Hyatt, N. C. *Nucl. Instru. Met. Phys. Res. B.* **2010**, *268***,** 1847-1852.

90. Salamat, A.; McMillan, P. F.; Firth, S.; Woodhead, K.; Hector, A. L.; Garbarino, G.; Stennett, M. C.; Hyatt, N. C. *J. Inorg. Chem*. **2013**, 52, 1550-1558.

91. Ringwood, A. E.; Kesson, S. E.; Ware, N. G.; Hibberson, W. O.; Major, A. *Geochem. J*. **1979**, 13, 141.

92. Lutze, W.; Grambow, B.; Ewing, R. C. *Nuclear Waste Forms.* **1989**, 847-851.

93. Sridhar, T. S.; Solomah, A. G. *Nucl. Tech.* **1989**, 85, 89-97.

94. Yang, J.; Tang, B.; Luo, S. MRS Proc. **2000**, 663, 333.

95. Lian, J.; Zu, X. T.; Kutty, K. V. G.; Chen, J.; Wang, L. M.; Ewing, R. C. Phys. Rev. B. **2002**, 66, 054108.

96. Lian, J.; Chen, J.; Wang, L. M.; Ewing, R. C. *Phys. Rev. B.* **2003**, *68*, 134107.

97. Arnold, G. W. *J. MRS*. **1985**, 44, 617.

98. Interface Science Western, http://www.isw.physics.uwo.ca/facilities_techniques/index.html.

99. Willmott, P. *An introduction to synchrotron radiation; Techniques and Applications*. A John Wiley & Sons Ltd: UK, **2011**.

100. Krinsky, S. *Fundamentals of hard X-ray synchrotron radiation sources., Third Generation Hard X-ray Synchrotron Radiation Sources*; John Wiley & Sons: New York, **2002**, 1–41.

101. Crease, R. P. *Phys. Perspect.* **2008**, 10, 438–467.

102. Liu, J.; Khater, H.; Prinz, A.; Rokni, S. *Synchrotron radiation shielding design*: Stanford Linear Accelerator Center, Stanford, CA; SLAC RP Note RP-03-08; **2003**.

103. Bokhoven, J. A. V.; Lamberti, C. *X-ray absorption and X-ray emission spectroscopy*: Wiley, UK, **2016**.

104. Koningsberger, D. C.; Prins, R. *X-ray Absorption: Principles and Application Techniques of EXAFS, SEXAFS and XANES:* Wyley, New York, **1988**.

105. Brown, G.S.; Doniach, S. *The principles of X-ray Absorption Spectroscopy*; Synchrotron Radiation Research: Plenum, NewYork, **1980**, 353–385.

106. Schnohr, C. S.; Ridgway, M. C. *Introduction to X-Ray Absorption Spectroscopy*. Springer series in optical sciences 190, **2015**.

107. Grant, S. H.; De Groot, F. M. F.; Moulton, B. J. A. *Mineralogy & Geochemistry*. **2014**, 78, 75-138.

108. Bunker, G. *Introduction to XAFS: a practical guide to X-ray absorption fine structure spectroscopy*, Cambridge University Press: Cambridge, U.K., **2010**.

109. Achkar, J.; Regier, T. Z.; Wadati, H.; Kim, Y. J.; Zhang, H.; Hawthorn, D. G.; *Phys. Rev. B* **2011**, 83, 081106-R.

110. Eisebitt, S.; Boske, T.; Rubensson, J. E.; Eberhardt, W. *Phys. Rev. B*. **1993**, 47, 14103-14109.

111. De Groot, F. M. F. *J. Electr. Spec. Relat. Phenom*. **1994**, 67, 529-622.

112. Troger, L. Arvanitis, D.; Baberschke, K.; Michaelis, H.; Grimm, U.; Zschech, E. *Phys. Rev. B*, **1992**, 46, 3283-3289.

113. Manceau, A.; Marcus, M. A.; Tamura, N. *Rev. Miner. Geochem.* **2002**, 49, 341-428.

114. De Groot, F. M. F. *Chem. Rev.* **2001**, 101, 1779-1808.

115. De Groot F. M. F. *Coord. Chem. Rev*. **2005**, 249, 31-63.

116. Grunes, L.A.; Leapman, R.D.; Wilker, C.N.; Hoffman, R.; Kunz, A.B. *Phys. Rev. B:Condens. Matter Mater. Phys.* **1982**, 25, 7157.

117. Wilke, M.; Farges, F.; Petit, P. E.; Brown; G. E.; Martin, F. *Am. Miner.* **2001**, 86, 714-730.

118. Farges, F.; Brown, G. E.; Rehr, J. J. *Phys. Rev. B: Condens. Matt.* **1997**, 56, 1809-1819.

119. Farges, F.; Brown, G. E.; Rehr, J. J. *Geochim. Cosmochim. Acta*. **1996**, 60, 3039-3055.

120. Grosvenor, A. P.; Greedan, J. E. *J. Phys. Chem. C.* **2009**, 113, 11366-11372.

121. Stennett, M. C.; Reid, D. P.; Peng, N.; Maddrell, E. R.; Ravel, B.; Hyatt, N. C. *Probing Radiation Damage in Ceramic Wasteforms Using X-ray Absorption Spectroscopy:* Budapest, Hungary, **2010**.

122. Waychunas, G. A. *Rev. Mineral. Geo. Chem.* **2002**, 49, 267.

123. Greaves, G. N.; Barrett, N. T.; Antonini, G. M.; Thornley, F. R.; Willis, B. T. M.; Steel, A. *Am. Chem. Soc.* **1989**, 111, 4313-4324.

124. PANalytical B. V. X'Pert HighScore Plus.Version 3.0; Almelo: Netherlands, **2011**.

125. Wallenberger, F. T.; Watson, J. C.; Li, H. *ASM: Composites*, **2001**, 21, 27-34.

126. Hrma, P.; Schweiger, M. J.; Humrickhouse, C. J.; Moody, J. A.; Tate, R. T.; Rainsdon, T. T.; TeGrotenhuis, N. E.; Arrigoni, B. M.; Marcial, J.; Rodriguez, C. P.; Tincher, B. H. *Ceramics – Silikáty*, **2010**, 54, 193-211.

127. Heald, S. M.; Brewe, D. L.; Stern, E. A.; Kim, K. H.; Brown, F. C.; Jiang, D. T.; Crozier, E. D.; Gordon, R. A. *J. Synchrotron Rad.* **1999**, 6, 347-349.

128. Aluri, E. R.; Hayes, J. R.; Walker, J. D. S.; Grosvenor, A. P. *J. Phys. Chem. C.* **2014**, 118, 7910-7922.

129. Thompson, A.; Attwood, D.; Gullikson, E.; Howells, M.; Kim, K. J.; Kirz, J.; Kortright, J.; Lindau, I.; Yanwei, L.; Pianetta, P.; Robinson, A.; Scofield, J.; Underwood, J.; Williams, G.; Winick, H. *X-ray Data Booklet*; Lawrence Berkeley National Laboratory: Berkeley, CA, **2001**.

130. Hu, Y. F.; Coulthard, I.; Chevrier, D.; Wright, G.; Igarashi, R.; Sitnikov, A.; Yates, B. W.; Hallin, E. L; Sham, T. K.; Reininger, R.; Garrett, R.; Gentle, I.; Nugent, K.; Wilkins, S. *AIP Conf. Proc.* **2010**, 1234, 343-346.

131. Hu, Y. F.; Zuin, L.; Reininger, R.; Sham, T. K. *AIP Conf. Proc.* **2007**, 879, 535-538.

132. Ravel, B.; Newville, M. *J. Synchrotron Rad.* **2005**, 12, 537-541.

133. Singh, J.; Singh, D.; Singh, S. P.; Mudahar, G. S.; Thind, K. *Mater. Phys. Mech.* **2014**, 9-15.

134. Sen, S.; Youngman, R. E. *J. Phys. Chem. B.* **2004**, 108, 7557-7564.

135. Zachariasen, W. H. *J. Am. Chem. Soc*. **1932**, 54, 3841–3850.

136. Zheng, Q. J.; Youngman, R. E.; Hogue, C. L.; Mauro, J. C.; Potuzak, M.; Smedskjaer, M. M.; Yue, Y. Z. *Phys. Rev. B.* **2012**, 86, 1-12.

137. Cabaret, D.; Joly, Y.; Renevier, H.; Natoli, C. R. *J. Synchrotron Rad.* **1999**, 6, 258-260.

138. Gaultois, M. W.; Grosvenor, A. P. *J. Mater. Chem.* **2011**, 21, 1829-1836.

139. Farges, F. *Am. Mineral.* **1997**, 82, 44-50.

140. Joly, Y.; Cabaret, D.; Renevier, H.; Natoli, C. R. *Phys. Rev. Lett.* **1999**, 82, 2398-2401.

141. Romano, C.; Paris, E.; Poe, B. T.; Giuli, G.; Dingwell, D. B.; Mottanai, A. *American Mineralogist.* **2000**, 85, 108-117.

142. Kotani, A.; Kvashnina, K.O.; Butorin, S.M.; Glatzel, P. *J. Electron. Spectrosc. Rel. Phenom.* **2011**, 184, 210-215.

143. Lopez, C.; Deschanels, X.; Bart, J. M.; Boubals, J. M.; Den Auwer, C.; Simoni, E. *J. Nucl. Mater.* **2003**, 312, 76-80.

144. Mountjoy, G.; Anderson, R.; Newport, R. J.; Smith, M. E. *J. Condens. Matter.* **2000**, 12, 3505-3519.

145. Gaultois, M. W.; Greedan, J. E.; Grosvenor, A. P. *J. Electron Spectroscopy and Related Phenomena.* **2011**, 184, 192-195.

146. Mountjoy, G.; Pickup, D. M.; Anderson, R.; Wallidge, G. W.; Holland, M. A.; Newport, R. J.; Smith, M. E. *J. Phys. Chem. Chem. Phys.* **2000**, 2, 2455-2460.

147. Jollivet, P.; Calas, G.; Galoisy, L.; Angeli, F.; Bergeron, B.; Gin, S.; Ruffoni, M. P.; Trcera, N. *Journal of Non-Crystalline Solids.* **2013**, 381, 40-47.

148. Patzig, C.; Höche, T.; Hu, Y.; Ikeno, H.; Krause, M.; Dittmer, M.; Gawronski, A.; Rüssel, C.; Tanaka, I.; Henderson, G. S. *Journal of Non-Crystalline Solids.* **2014**, 384, 47-54.

149. Li, D.; Bancroft, G. M.; Kasrai, M.; Fleet, M. E.; Feng, X. H.; Tan, K. H.; Yang, B. X. *Solid State Commun.* **1993**, 87, 613-617.

150. Li, D.; Bancroft, G. M.; Kasrai, M.; Fleet, M. E.; Secco, R. A.; Feng, X. H.; Tan, K. H.; Yang B. X. *Am. Mineral*. **1994**, 79, 622-632.

151. Garvie, L. A. J.; Buseck, P. R. *Am. Mineral.* **1999**, 84, 946-964.

152. Harp, G. R.; Saldin, D. K.; Tonner, B. P. *J. Condens. Matter.* **1993**, 5, 5377-5388.

153. Sammynaiken, R.; Naftel, S. J.; Sham, T. K.; Cheah, K. W.; Averboukh, B.; Huber, R. Shen, Y. R.; Qin, G, G.; Ma, Z. C.; Zong, W. H. *Journal of applied physics*. **2002**, 92, 3000-3006.

154. Hayes J. R.; Grosvenor, A. P. *J. Alloys Comp.* **2012**, 537, 323-331.

155. Sigrist, J. A.; Gaultois M. W.; Grosvenor, A. P. *J. Phys. Chem. A.* **2011**, 115, 1908-1912.

156. Westre, T. E.; Kennepohl, P.; Dewitt, J. G.; Hedman, B.; Hodgson K. O.; Solomon, E. I. *J. Am. Chem. Soc.* **1997**, 119, 6297-6314.

157. Magnien, V.; Neuville, D. R.; Cormier, L.; Roux, J.; Hazemann, J. L.; Pinet, O.; Richet, P. *J. Nucl. Mater.* **2006**, 352, 190-195.

158. Mehdikhani, B.; Borhani, G. H. *Process. Appl. Ceram.* **2013**, 7, 117-121.

159. Magnien, V.; Neuville, D. R.; Cormier, L.; Roux, J.; Hazemann, J. L.; de Ligny, D.; Pascarelli, S.; Vickridge, I.; Pinet, O.; Richet, P. *Geo. Cosmo. Acta.* **2008**, 72, 2157-2168.

160. Walker, J. D. S.; Grosvenor, A. P. *Inorg. Chem.* **2013**, 52, 8612-862

161. H. H. Andersen, H. H. *Appl. Phys*. **1979**, 18, 131.

162. Ziegler, J. F.; Biersack, J. P.; Ziegler, M. D. *SRIM (The Stopping and Range of Ions in Solids)*, MD: USA, **2013**.

163. Smyth, J. R.; McCormick. T. C.; *Mineral Physics and Crystallography*: A Handbook of Physical Constants, **1995**.

164. X-ray Attenuation Length. http://henke.lbl.gov/optical_constants/atten2.html.

165. Chatzistavrou, X.; Esteve, D.; Hatzistavrou, E.; Kontonasaki, E.; Paraskevopoulos, K. M.; Boccaccini, A. R. *Journal of Bioceramics Development and Applications*. **2011**, 1, 1-4.

166. McGann, O. J.; Gandy, A. S.; Bingham, P. A.; Hand, R. J.; Hyatt, N. C. *MRS Proc.* **2013**, 1518, 41-46.

167. Magnien, V.; Neuville, D. R.; Cormier, L.; Roux, J.; Hazemann, J. L.; Pinet, O.; Richet, P. *J. Nucl. Mater.* **2006**, 352, 190-195.

168. Zhang, H.; Corkhill, C. L.; Heath, P. G.; Hand, R. J.; Stennett, M. C.; Hyatt, N. C. *J. Nucl. Mater.* **2015**, 462, 321–328.

Appendix A1

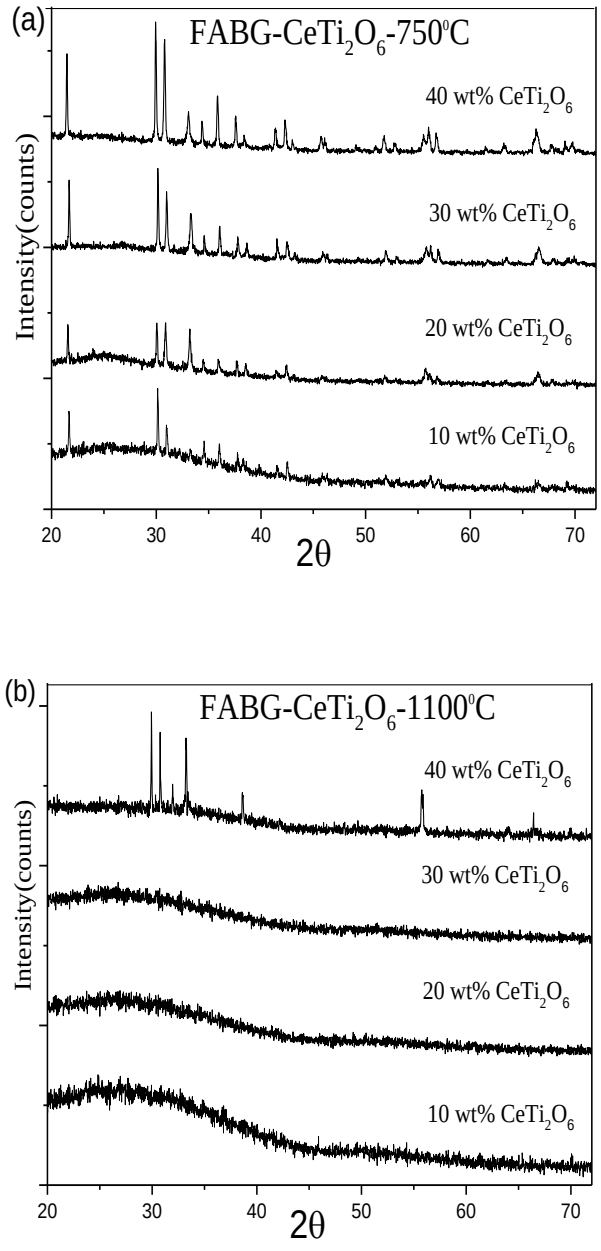

Figure A1.1. XRD patterns from the composite materials containing 10, 20, 30, and 40 wt% loading of $CeTi_2O_6$ in Fe-Al borosilicate glass annealed at (a) 750 or (b) 1100 ^oC are shown.

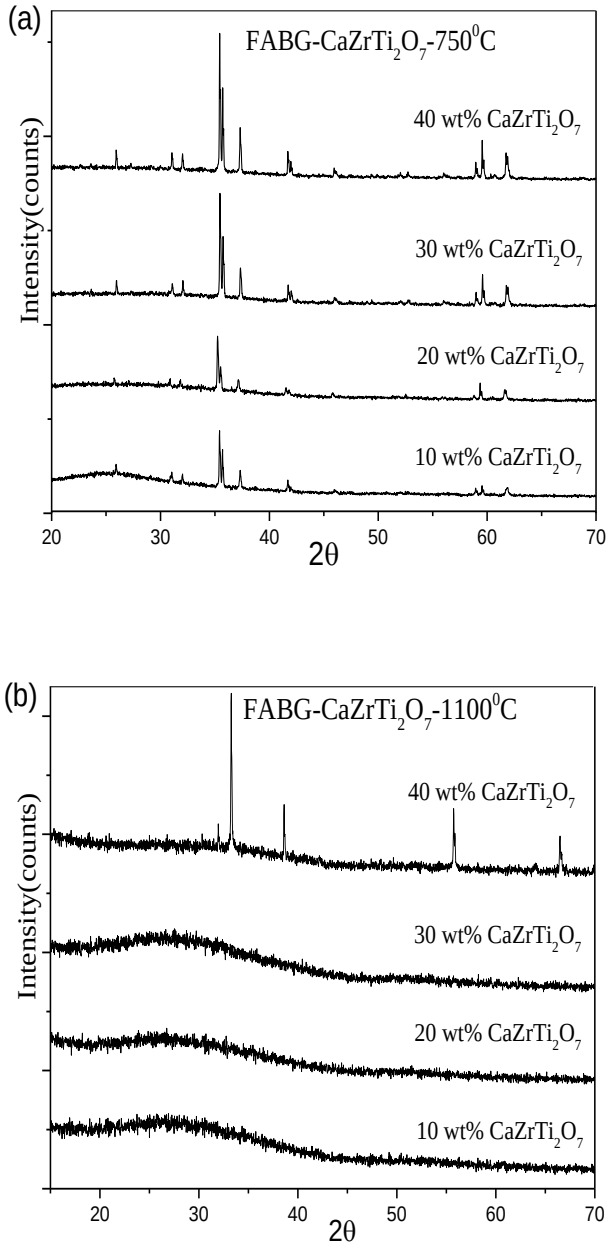

Figure A1.2. XRD patterns from the composite materials containing 10, 20, 30, and 40 wt% loading of $CaZrTi_2O_7$ in Fe-Al borosilicate glass annealed at (a) 750 or (b) 1100 ^oC are shown.

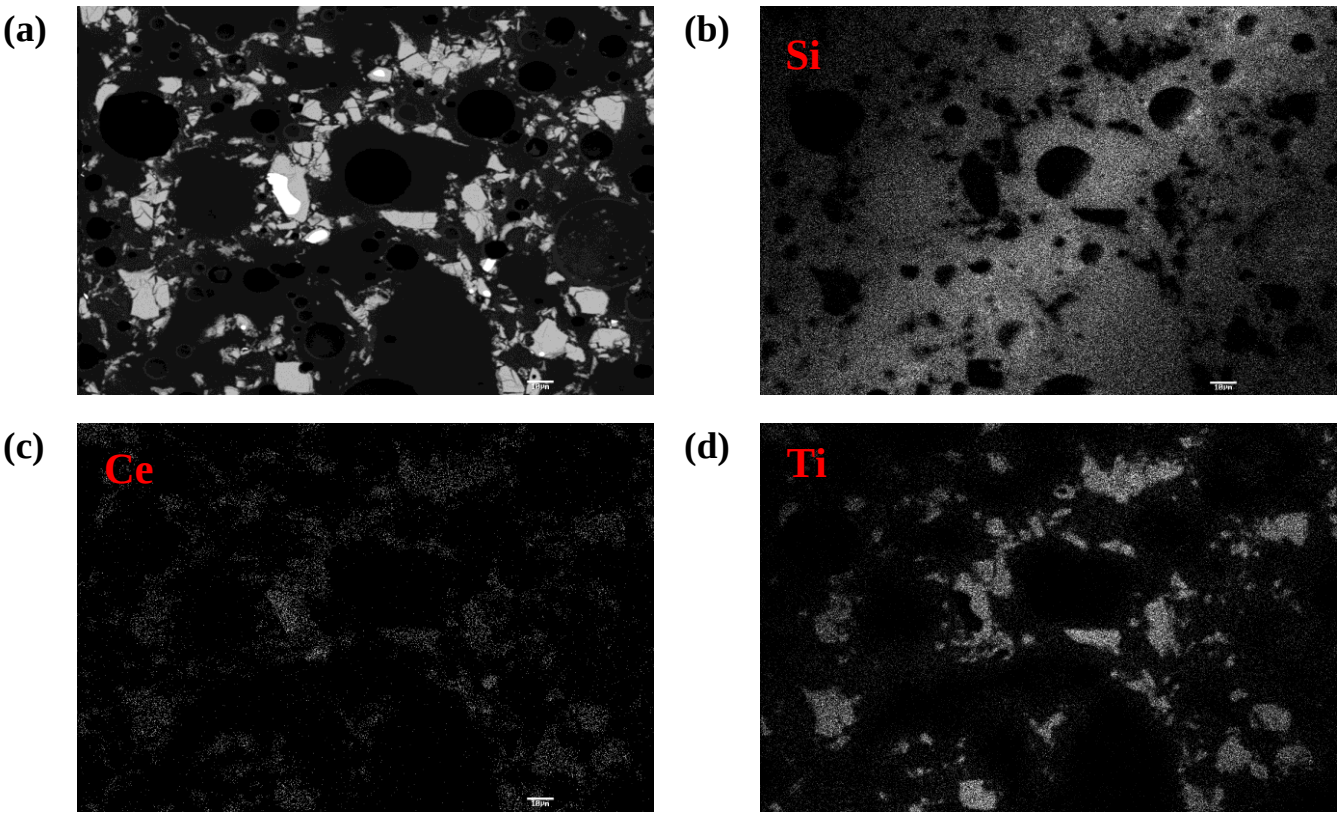

Figure A1.3. (a) A backscattered image and EDX maps of (b) Si, (c) Ce, and (d) Ti from the composite material containing 30 wt% loading of $CeTi_2O_6$ in borosilicate glass annealed at 750 ºC are shown. The scale bar in each image is 10 µm.

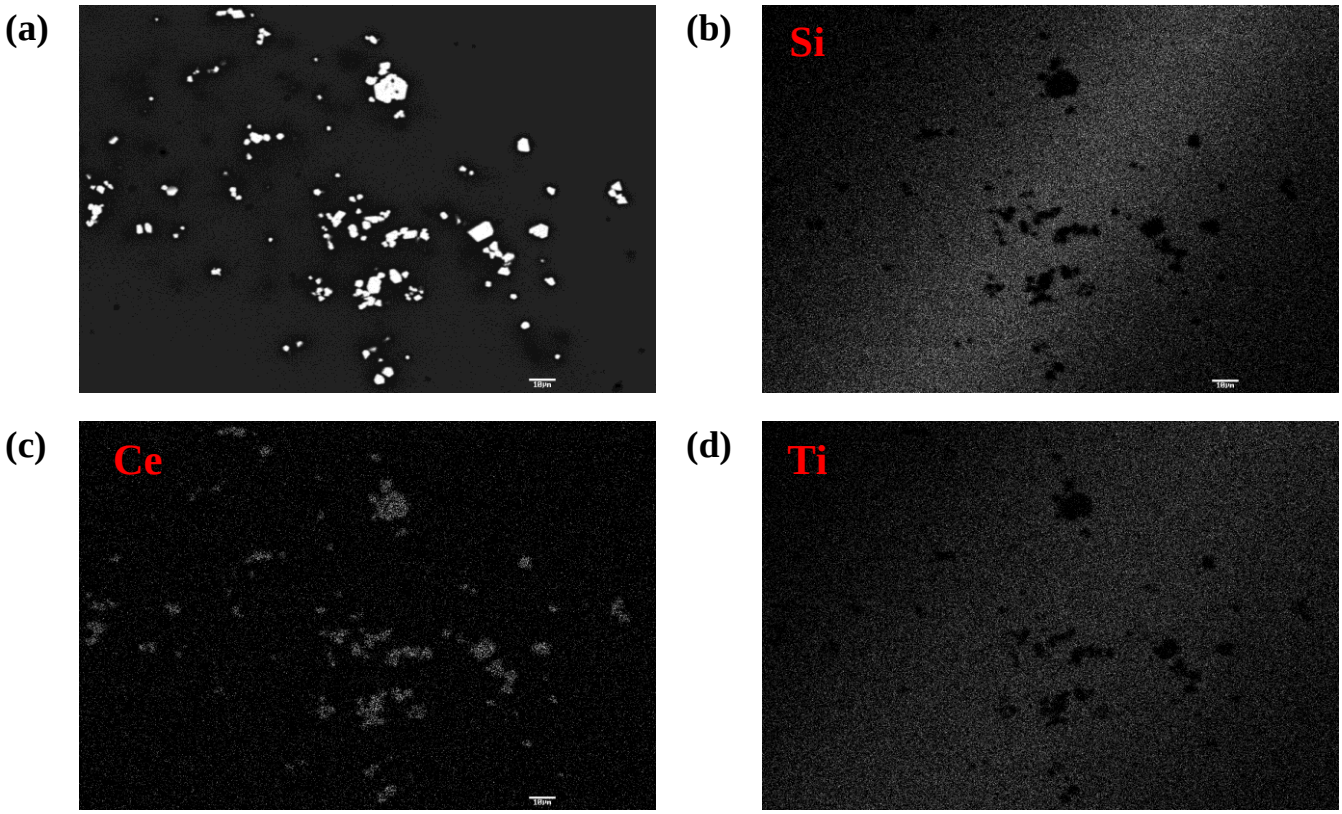

Figure A1.4. (a) A backscattered image and EDX maps of (b) Si, (c) Ce, and (d) Ti from the composite material containing 30 wt% loading of $CeTi_2O_6$ in borosilicate glass annealed at 1100 ^oC are shown. The scale bar in each image is 10 μm.

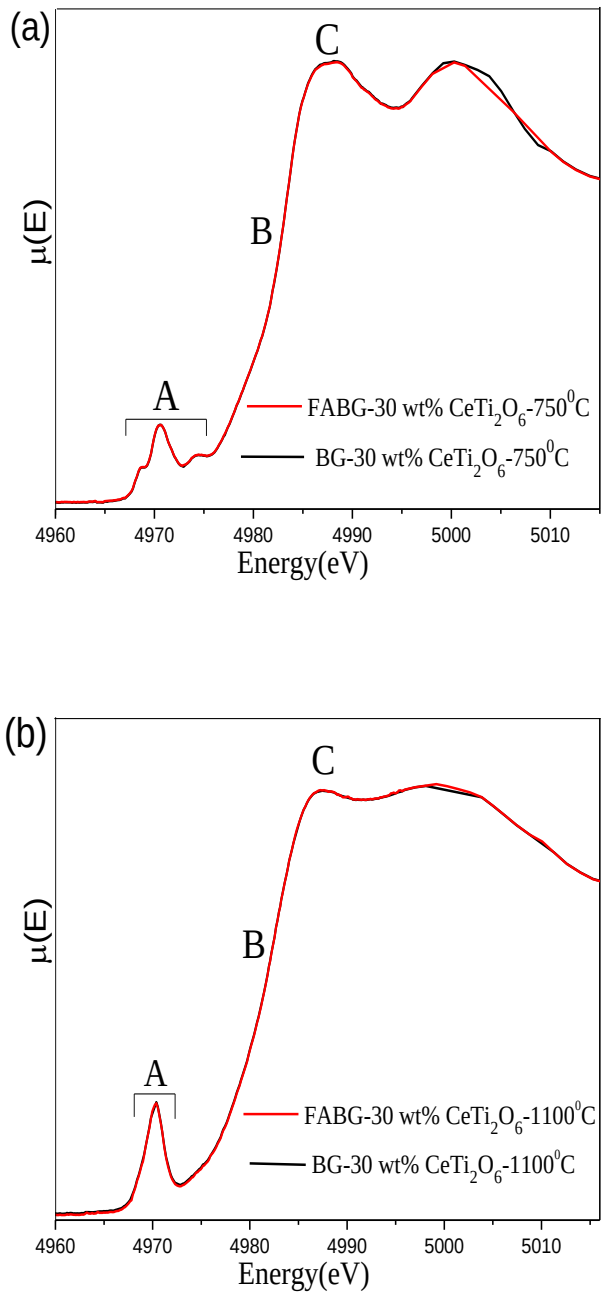

Figure A1.5. Ti K-edge XANES spectra from borosilicate glass and Fe-Al borosilicate glass composite materials containing a 30 wt% loading of $CeTi_2O_6$ annealed at (a) 750 or (b) 1100 ^oC are shown.

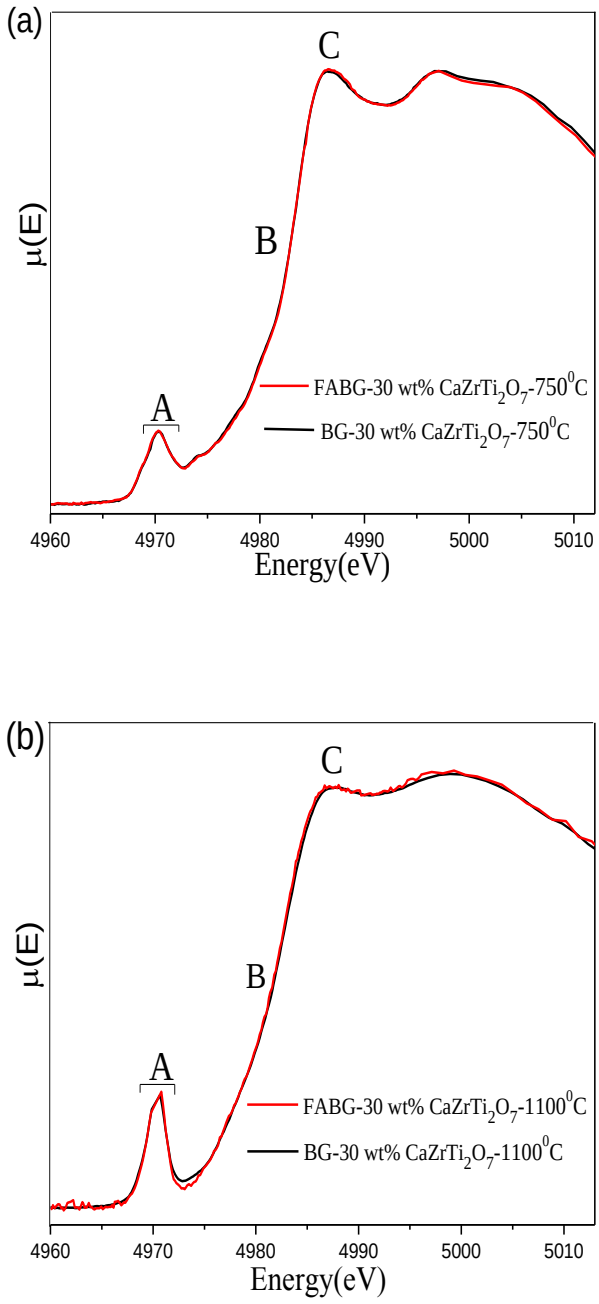

Figure A1.6. Ti K-edge XANES spectra from borosilicate glass and Fe-Al borosilicate glass composite materials containing a 30 wt% loading of $CaZrTi_2O_7$ annealed at (a) 750 or (b) 1100 ºC are shown.

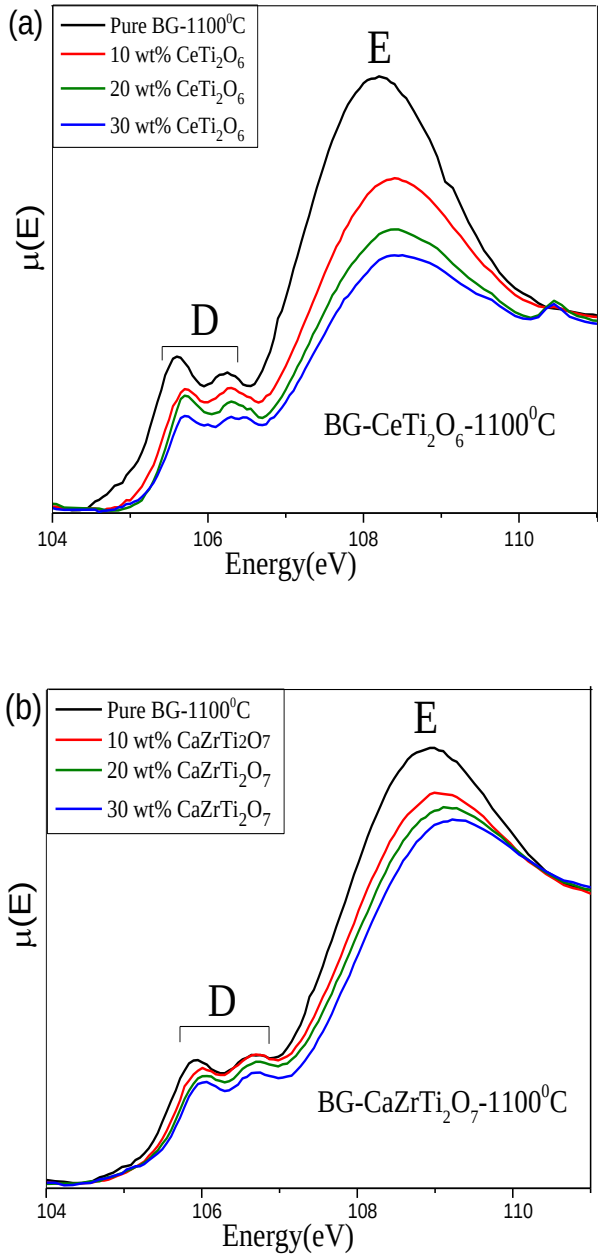

Figure A1.7. Si $L_{2,3}$-edge XANES spectra from (a) BG-$CeTi_2O_6$-1100 ºC containing 10, 20 and 30 wt% loading of $CeTi_2O_6$ and (b) BG-$CaZrTi_2O_7$-1100 ºC containing 10, 20, and 30 wt% loading of $CaZrTi_2O_7$ are shown. The spectra are compared to the spectrum from borosilicate glass.

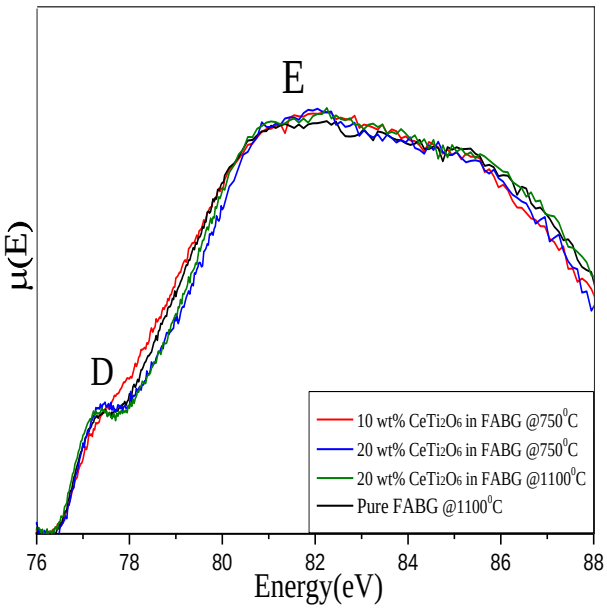

Figure A1.8. Al $L_{2,3}$-edge XANES spectra from the composite materials containing 10 and 20 wt% loading of $CeTi_2O_6$ in Fe-Al borosilicate glass annealed at 750 ºC and 20 wt% loading of $CeTi_2O_6$ in Fe-Al borosilicate glass annealed at 1100 ºC are shown. The spectrum from the Fe-Al borosilicate glass is also presented.